
Article:
Rudolph, D., Andreoiu, C., Bentley, M. A. orcid.org/0000-0001-8401-3455 et al. (9 more authors) (2021) Experimental and shell-model study of excited states in and related notes on. Physical Review C. 044314. ISSN 2469-9993

https://doi.org/10.1103/PhysRevC.104.044314

Experimental and shell-model study of excited states in $^{55}_{26}Fe_{29}$ and related notes on $^{55}_{29}Cu_{26}$

D. Rudolph,[1,*] C. Andreoiu,[1,2] M. A. Bentley,[3] M. P. Carpenter,[4] R. J. Charity,[5] R. M. Clark,[6] J. Ekman,[1,7] C. Fahlander,[1] P. Fallon,[6] W. Reviol,[4,5] D. G. Sarantites,[5] and D. Seweryniak[4]

[1]*Department of Physics, Lund University, S-22100 Lund, Sweden*
[2]*Chemistry Department, Simon Fraser University, Burnaby, BC, Canada V5A 1S6*
[3]*Department of Physics, University of York, Heslington, York YO10 5DD, England, United Kingdom*
[4]*Physics Division, Argonne National Laboratory, Argonne, Illinois 60439, USA*
[5]*Chemistry Department, Washington University, Saint Louis, Missouri 63130, USA*
[6]*Nuclear Science Division, Lawrence Berkeley National Laboratory, Berkeley, California 94720, USA*
[7]*Department of Materials Science and Applied Mathematics, Malmö University, S-20506 Malmö, Sweden*

(Received 6 August 2021; accepted 29 September 2021; published 13 October 2021)

The fusion-evaporation reaction $^{32}S + ^{28}Si$ at 125-MeV beam energy was used to populate excited states in ^{55}Fe. Combining the Gammasphere spectrometer with ancillary devices including the Microball CsI(Tl) array and a shell of neutron detectors, a comprehensive level scheme could be derived. The experimental results are compared with theoretical results from shell-model calculations. Taking into account isospin-symmetry breaking terms is found to considerably improve the shell-model description for ^{55}Fe. This motivated a predictive case study of near-yrast states in the mirror nucleus ^{55}Cu.

DOI: 10.1103/PhysRevC.104.044314

I. INTRODUCTION

Doubly magic nuclei and their nearby neighbors are unique laboratories to test and improve predictions from shell-model calculations [1,2]. Spectroscopic data from these nuclei put the most severe constraints on the outcome of such calculations and, consequently, help to define and relate the effective nuclear forces by probing parameters such as single-particle energies and two-body matrix elements.

The spherical shell gap at $N = Z = 28$ (^{56}Ni) is created by the spin-orbit splitting of the $0f$ shell, separating the $0f_{7/2}$ orbital from the so-called upper fp shell, which is composed of its $0f_{5/2}$ spin-orbit partner as well as the $1p_{3/2}$ and $1p_{1/2}$ orbitals. The possibility for both $f_{7/2}$-$f_{5/2}$ magnetic-dipole ($M1$) and $f_{7/2}$-$p_{3/2}$ electric-quadrupole ($E2$) correlations across the gap makes ^{56}Ni a soft core; the ground state has a rather low ≈50% closed-core partition [3]. Furthermore, a proton-neutron symmetric four-particle four-hole ($4p$-$4h$) excitation gives rise to a second, prolate deformed shell gap at $N = Z = 28$, which is reinforced by excitations into the $0g_{9/2}$ intruder orbital. The respective spherical-prolate shape coexistence has been observed [4–6] and predicted [4,7] in ^{56}Ni itself and neighboring nuclei. For example, the ^{58}Ni level scheme reaches record-high excitation energies and rotational frequencies [8], it is one of the most comprehensive across the nuclear chart [9], and it includes discrete-energy proton and α-particle emissions into ^{57}Co and ^{54}Fe, respectively, which compete with electromagnetic radiation on the picosecond time scale.

In recent years, it has become computationally feasible to perform unrestricted $0\hbar\omega$ shell-model calculations in the full $\mathcal{N} = 3$ fp shell [10]. In conjunction with effective [11,12] or only marginally empirical [13] interactions of high spectroscopic quality, certainly for nuclei with $N, Z < 28$, it has also been possible to conduct detailed studies on isospin symmetry by using energy differences of excited analog states in mirror nuclei [14,15].

The present study of $^{55}_{26}Fe_{29}$ was motivated by the search for single-particle or collective excitations engaging the $g_{9/2}$ intruder orbital, similar to those observed in neighboring odd-A isotopes, for example, $^{57}_{28}Ni_{29}$ [16–18], $^{57}_{27}Co_{30}$ [19,20], or $^{53}_{25}Mn_{28}$ [21]. Furthermore, as mentioned earlier, comprehensive and detailed spectroscopic information on $A \gtrsim 50$, $N > 28$ nuclei is required to possibly and reliably track anticipated drip-line effects in their neutron-deficient mirror partners with $N < Z$, $Z > 28$. These are in experimental reach at existing and upcoming fragmentation facilities, especially by means of one- or two-nucleon knockout reactions [22–24].

First γ-ray spectroscopic studies along the yrast line of ^{55}Fe were conducted by means of α- or ^{7}Li-induced reactions [25,26], later confirmed by heavy-ion induced fusion-evaporation reactions [27,28]. Lifetimes of some yrast states were measured with Doppler-shift techniques [26,29], and a few gyromagnetic factors could be determined as well [30]. For more comprehensive information on excited states in ^{55}Fe and their γ-ray decay pattern, we refer to evaluated data files [31,32].

*Dirk.Rudolph@nuclear.lu.se

Section II briefly describes the experimental background, and Sec. III summarizes tools and methods of the data analysis. The experimental results are reported in Sec. IV. Section V presents an interpretation of the ^{55}Fe level scheme in the framework of contemporary large-scale shell-model calculations, without and with the inclusion of isospin symmetry breaking terms. The latter considerably improve the description of ^{55}Fe and inspire corresponding calculations in the mirror nucleus $^{55}_{29}Cu_{26}$, described in Sec. VI.

II. EXPERIMENT

The present paper is based on a combined data set from two experiments. They were conducted under almost identical conditions at the Argonne Tandem-Linac Accelerator System (ATLAS) at Argonne National Laboratory (ANL) and the 88-inch Cyclotron at Lawrence Berkeley National Laboratory (LBNL). In both experiments the fusion-evaporation reaction ^{32}S + ^{28}Si was used to populate high-spin states in neutron-deficient mass $A \approx 50$–60 nuclei. The ^{32}S beam ions of 125 MeV impinged onto the ^{28}Si target. The isotopic enrichment of the target material was 99.90%, and the ^{28}Si target layer had a thickness of 0.5 mg/cm^2, which was evaporated on 1-mg/cm^2 foils of either gold or tantalum. These thin support foils faced the incoming beam. Furthermore, a part of the experiment at LBNL used a ^{28}Si target layer backed by 13-mg/cm^2 tantalum. In this case, the beam impinged directly onto the ^{28}Si layer, and the recoiling reaction products were stopped inside the tantalum backing. This allowed for high-resolution spectroscopy of those parts of level schemes located below states with effective lifetimes $\tau \gtrsim 1$ ps, which corresponds to the typical time it took to stop the recoils in the tantalum backing. Excited states in ^{55}Fe were populated following the evaporation, from the compound nucleus ^{60}Zn, of four protons and one neutron, i.e., the $4p1n$ channel was investigated.

The Gammasphere array [33] surrounded the target chamber. The array was composed of 78 Compton-suppressed Ge-detector modules at the time of both experiments, used to detect the emitted prompt γ rays. The heavimet collimators, usually used to protect the Gammasphere anti-Compton shields from direct γ radiation, were removed to allow for γ-ray multiplicity and sum-energy measurements. This has proven particularly useful for studies along the $N \approx Z$ line, where reaction-channel selection capabilities are among the most crucial experiment parameters. Therefore, the 4π CsI-array Microball [34] was mounted inside the target chamber. It served the detection of evaporated light charged particles. In addition, the Neutron Shell [35] was used, i.e., 30 liquid-scintillator detectors of hexagonal shape replaced the 30 most forward Gammasphere modules. Its prime use was to select weak reaction channels involving one- or even two-neutron evaporation approaching or crossing the $N = Z$ line. For the present study of ^{55}Fe, the active detection of the evaporated neutron suppressed practically all γ radiation from the otherwise dominating $4p$ reaction channel, namely, ^{56}Fe.

Two conditions were set to collect coincidence events in list mode: Either four or more Ge detectors were required to fire, or three or more Ge detectors plus one or more neutron detectors. Calibration data for Gammasphere were taken with standard ^{56}Co, ^{133}Ba, and ^{152}Eu sources. Furthermore, during the experiment the $\tau = 525$ ns, $I^\pi = 10^+$ isomer in ^{54}Fe was populated with rather high yield [21]. Most of the ^{54}Fe recoils stopped in Microball absorber foils. Therefore, the five-γ-long $E2$ cascade from the isomer decay could be used to monitor potential Ge-detector signal drift throughout the experiments and across the γ-ray energy range of interest ($\approx$0.1–4.0 MeV). Energy calibrations of Microball detector elements were based on scattering data from ^{12}C(p, p') and ^{197}Au(α, α') reactions.

III. DATA ANALYSIS

The details of the data analysis of this type of experiments have been described earlier; for the present data sets, see, for example, Refs. [36–38] and references therein. In brief, γ-ray spectra in prompt coincidence with the relevant numbers and kinds of evaporated particles were generated, here four protons and one neutron. Pulse-shape discrimination techniques were used to distinguish between protons and α particles detected in Microball and to separate neutrons from γ rays detected in the Neutron Shell. The particle detection efficiencies were determined to be $\approx$65% for protons, $\approx$50% for α particles, and $\approx$25% for neutrons for the combined data set used in this paper. An event-by-event kinematic reconstruction method used the measured energies and directions of the detected evaporated particles to determine the momentum vector of the excited residues. Thus, an event-by-event Doppler correction was performed to correct the γ-ray spectra for Doppler broadening caused by the evaporated particles.

The list mode data were converted into E_γ-E_γ matrices and E_γ-E_γ-E_γ cubes correlated with four protons and one neutron. These objects, and their projected γ-ray spectra, were inspected with the help of the Radware software package [39] and the spectrum-analysis code TV [40]. Two $4p1n$-channel selected E_γ-E_γ matrices were the main source of information when establishing $\gamma\gamma$ coincidence relations, which resulted in the high-spin level scheme of ^{55}Fe shown in Fig. 1. The matrix for the combined thin-target experiments contained 2.3×10^6 entries, with $\gtrsim$95% of them associated with ^{55}Fe. The matrix for the backed-target run contained 3.4×10^5 entries, with $\gtrsim$90% associated with ^{55}Fe.

Minor contaminations in the $4p1n$-gated spectra could arise, for example, from the $3p1n$ and $3p2n$ channels ^{56}Co and ^{55}Co through rare random detection of a fourth proton. For the backed-target run, a negligible amount of random coincidences with γ rays from Coulomb excited ^{181}Ta were present. Note that the well-known main decay sequences of these isotopes did not affect the analysis of ^{55}Fe. Moreover, these contaminants could be suppressed by applying the total energy plane selection method [41].

Multipolarity assignments of γ-ray transitions were based on directional correlations of oriented states (DCO ratios). The analysis procedure followed the one outlined in Ref. [16] and applied in many subsequent publications; see, e.g., Refs. [36,38] concerning the present data sets. DCO ratios

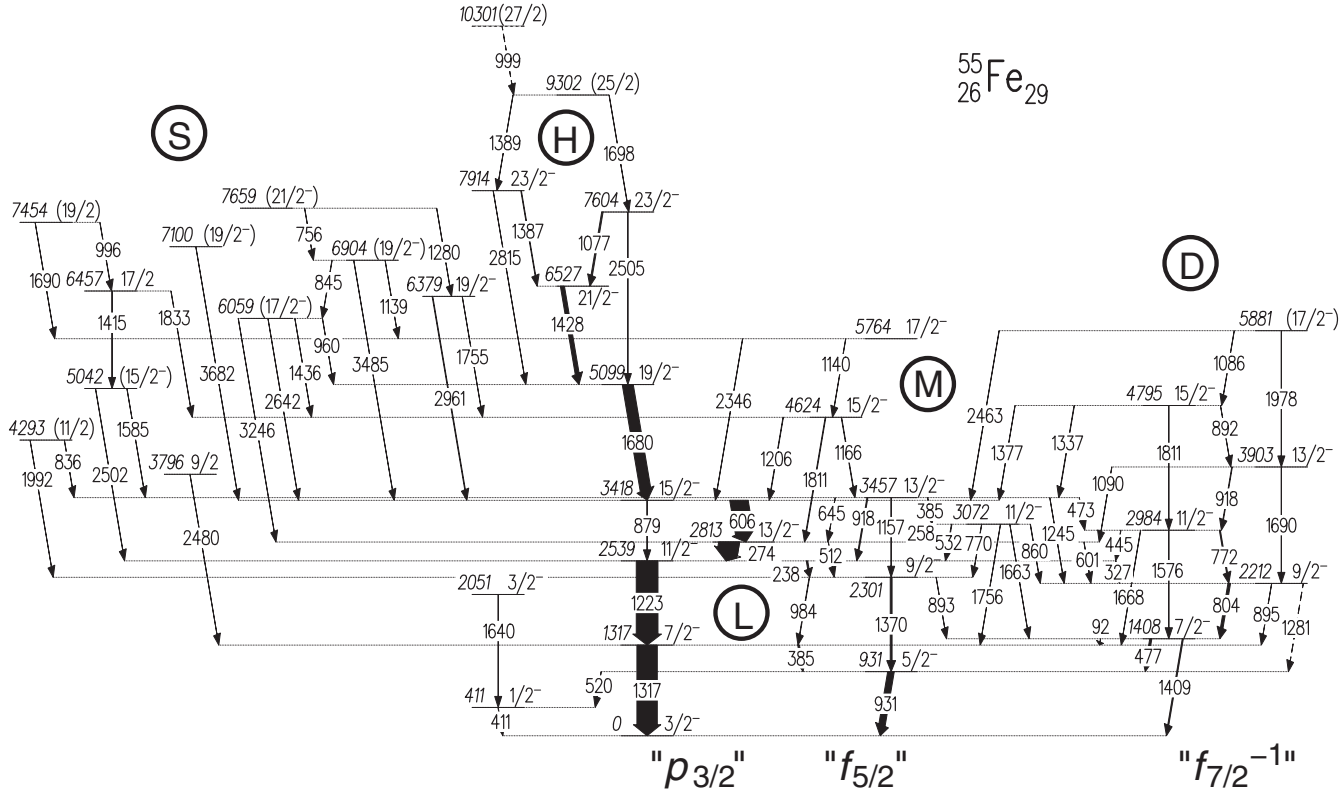

FIG. 1. Proposed level scheme of ^{55}Fe from the present paper. Energy labels are in keV. Tentative transitions and levels are dashed. The widths of the arrows correspond to the relative intensities of the γ rays. Encircled letters denote parts of the level scheme as presented in Sec. IV. To ease the connection with the theoretical discussion (see Sec. V and Fig. 6), orbital descriptors in quotation marks are indicative for the location of the odd neutron for the respective set of states.

were thus derived according to

$$R_{\mathrm{DCO}}(150\text{-}97) = \frac{I(\gamma_1 \text{ at } 150^\circ; \text{gated with } \gamma_2 \text{ at } 97^\circ)}{I(\gamma_1 \text{ at } 97^\circ; \text{gated with } \gamma_2 \text{ at } 150^\circ)}.$$

The method used 15 germanium detectors at 163°, 148°, and 143° with $\langle\theta_1\rangle = 150^\circ$ relative to the beam axis and 28 detectors at 80°–100° with $\langle\theta_2\rangle = 97^\circ$ relative to the beam axis. Note the underlying symmetry of angular distribution and correlation measurements with respect to a reaction plane at 90° relative to the beam axis.

Only known stretched $E2$ transitions ($\Delta I = 2$, $I \rightarrow I$-2) were used as gating transitions. In this case one expects $R_{\mathrm{DCO}} = 1.0$ for observed stretched $E2$ transitions and $R_{\mathrm{DCO}} \approx 0.6$ for stretched pure $\Delta I = 1$, $I \rightarrow I$-1 dipole transitions. Nonstretched $\Delta I = 0$ transitions are expected to have values similar to $E2$ transitions. Deviations from the estimates for pure $\Delta I = 1$ transitions indicate a finite mixing ratio of the respective transition, namely, $\delta(E2/M1) > 0$ (< 0) for numbers smaller (larger) than expected for R_{DCO}(150–97). Furthermore, from a parallel decay sequence or from yrast arguments constraints can be invoked to resolve initially ambiguous spin-parity assignments. As a general guideline in fusion-evaporation reactions, the more intensity a transition carries, the closer it is to the yrast line.

IV. EXPERIMENTAL RESULTS

The experimental information for excited states in ^{55}Fe and their decay is summarized in Table I. This includes relative intensities and energies of the γ-ray transitions as well as excitation energies and assigned spins and parities of the excited states. The level scheme of ^{55}Fe is illustrated in Fig. 1. Five distinctive regions are considered, indicated with letters: the previously established low-spin (L) and high-spin (H) yrast sequences in the center of Fig. 1, an extended dipole structure (D) placed on the right-hand side, an intermediate region (M) between structures L and D, and a number of side structures (S) on the left-hand side.

The level scheme is extended beyond previous work [31], in particular in width, i.e., the number of non-yrast levels and connecting transitions has increased, primarily in regions D, M, and S. Only marginal corrections with respect to previous work are suggested. These find specific mentioning in the following, also in relation to the latest evaluation of mass $A = 55$ nuclei [31] and the respective information available in the Evaluated Nuclear Structure Data File [32].

A. The yrast sequences (L and H)

The low-spin yrast sequence up to the $15/2^-_1$ state at 3418 keV is consistent with previous work. It cascades mainly by two intense, stretched, and almost pure $M1$ transitions of

TABLE I. Energy levels in ^{55}Fe, the transition energies and relative intensities of the γ rays placed in the level scheme, their DCO ratios and multipole assignments, and the derived spins and parities of the initial and final states of the γ rays.

E_x (keV)	E_γ[a] (keV)	$I_{\rm rel}$ (%)	Gate[b]	$R_{\rm DCO}$ 150°–97°	Mult. ass.	I_i^π ($\hbar$)	I_f^π ($\hbar$)
411.3(2)	*411.3(3)*	13(1)			$M1$[c]	$1/2_1^-$[c]	$3/2_1^-$
931.2(1)	*519.9(2)*	5(1)			$E2$[c]	$5/2_1^-$	$1/2_1^-$
	931.2(1)	294(9)	B,D	1.00(10)	$E2/M1$[c]	$5/2_1^-$[c]	$3/2_1^-$
1316.5(1)	*385.4(2)*	77(3)	*B,C*	0.47(5)	$M1$	$7/2_1^-$	$5/2_1^-$
	1316.5(1)	939(28)	*B,C*	0.99(5)	$E2$	$7/2_1^-$	$3/2_1^-$
1408.4(1)	91.9(2)[d]	6(1)			$\Delta I = 0$	$7/2_2^-$[c]	$7/2_1^-$
	477.2(1)	93(3)	F	0.51(18)	$E2/M1$	$7/2_2^-$	$5/2_1^-$
	1408.5(1)	49(2)	F	1.09(43)	$E2$	$7/2_2^-$	$3/2_1^-$
2051.4(12)	1640.2(12)	2(1)			$E2/M1$[c]	$3/2_2^-$[c]	$1/2_1^-$
2212.1(2)	*803.7(2)*	117(4)	E	0.53(9)	$E2/M1$	$9/2_1^-$	$7/2_2^-$
	894.6(8)	4(1)	A	<1[e]	$E2/M1$	$9/2_1^-$	$7/2_1^-$
	1280.6(15)	2(1)			$E2$	$9/2_1^-$	$5/2_1^-$
2301.0(1)	892.6(8)	4(1)	E	$\ll 1$[e]	$E2/M1$	$9/2_2^-$	$7/2_2^-$
	984.4(3)	19(1)	A	1.65(63)	$E2/M1$	$9/2_2^-$	$7/2_1^-$
	1369.8(1)	84(3)	C	0.96(30)	$E2$[c]	$9/2_2^-$	$5/2_1^-$
2539.2(1)	*238.3(1)*	64(2)	D	0.59(9)	$E2/M1$	$11/2_1^-$	$9/2_2^-$
	327.2(2)	10(1)			$E2/M1$	$11/2_1^-$	$9/2_1^-$
	1222.7(1)	1000(30)	*A,C*	1.03(5)	$E2$	$11/2_1^-$	$7/2_1^-$
2812.8(1)	*273.6(1)*	932(28)	*A,B,C*	0.54(3)	$E2/M1$	$13/2_1^-$	$11/2_1^-$
	511.7(4)	5(1)	D	≈ 1	$E2$	$13/2_1^-$	$9/2_2^-$
	600.5(2)	7(1)			$E2$	$13/2_1^-$	$9/2_1^-$
2984.2(3)	445.1(4)	10(1)			$\Delta I = 0$	$11/2_2^-$	$11/2_1^-$
	772.0(4)	46(2)	E	0.55(15)	$E2/M1$	$11/2_2^-$	$9/2_1^-$
	1575.6(11)	15(1)	E	≈ 1	$E2$	$11/2_2^-$	$7/2_2^-$
	1667.5(12)	7(1)			$E2$	$11/2_2^-$	$7/2_1^-$
3071.6(2)	*258.3(3)*	8(1)	*B*	0.40(17)	$E2/M1$	$11/2_3^-$	$13/2_1^-$
	532.4(2)	24(1)	*B*	0.92(32)	$\Delta I = 0$	$11/2_3^-$	$11/2_1^-$
	770.4(4)	8(1)			$E2/M1$	$11/2_3^-$	$9/2_2^-$
	859.6(5)	10(1)			$E2/M1$	$11/2_3^-$	$9/2_1^-$
	1662.8(11)	4(1)			$E2$	$11/2_3^-$	$7/2_2^-$
	1755.8(13)	3(1)			$E2$	$11/2_3^-$	$7/2_1^-$
3418.4(2)	*605.6(1)*	822(25)	*A,B,C*	0.53(3)	$E2/M1$	$15/2_1^-$	$13/2_1^-$
	879.0(3)	12(1)			$E2$	$15/2_1^-$	$11/2_1^-$
3457.2(2)	*385.4(2)*	20(2)	A	0.54(27)	$E2/M1$	$13/2_2^-$	$11/2_3^-$
	472.7(5)	8(1)	[e]		$E2/M1$	$13/2_2^-$	$11/2_2^-$
	644.9(5)	3(1)			$\Delta I = 0$	$13/2_2^-$	$13/2_1^-$
	917.8(4)	42(3)	A,B	0.60(8)	$E2/M1$	$13/2_2^-$	$11/2_1^-$
	1156.8(9)	2(1)	D	1.00(46)	$E2$	$13/2_2^-$	$9/2_2^-$
	1245.3(9)	2(1)			$E2$	$13/2_2^-$	$9/2_1^-$
3796.1(21)	2479.6(21)	2(1)	A	0.63(25)	$\Delta I = 1$	9/2	$7/2_1^-$
3902.6(4)	918.4(5)	26(2)	E,F	0.46(23)	$E2/M1$	$13/2_3^-$	$11/2_2^-$
	1089.6(8)	6(1)	B	1.16(33)	$\Delta I = 0$[e]	$13/2_3^-$	$13/2_1^-$
	1690.2(12)	9(1)	E	≈ 1	$E2$	$13/2_3^-$	$9/2_1^-$
4293.0(7)	835.8(7)	7(1)	A+B	$\ll 1$	$(\Delta I = 1)$	$(11/2_4)$	$13/2_2^-$
	1991.9(15)	3(1)			$(\Delta I = 1)$	$(11/2_4)$	$9/2_2^-$
4623.8(5)	1166.2(8)	18(1)	A+B	<1	$E2/M1$	$15/2_2^-$	$13/2_2^-$
	1205.9(8)	18(1)			$\Delta I = 0$	$15/2_2^-$	$15/2_1^-$
	1811.1(11)	29(2)	A+B	0.66(23)	$E2/M1$	$15/2_2^-$	$13/2_1^-$
4794.9(6)	892.3(6)	5(1)	E	$\ll 1$[e]	$E2/M1$	$15/2_3^-$[f]	$13/2_3^-$
	1337.4(12)	16(1)			$E2/M1$	$15/2_3^-$	$13/2_2^-$
	1376.6(15)	6(2)			$\Delta I = 0$	$15/2_3^-$	$15/2_1^-$
	1810.9(14)	4(1)			$E2$	$15/2_3^-$	$11/2_2^-$
5041.8(9)	1584.8(12)	3(1)			$(E2/M1)$	$(15/2_4^-)$[f]	$13/2_2^-$
	2502.0(20)	8(1)	A+B	0.86(39)	$(E2)$	$(15/2_4^-)$	$11/2_1^-$
5098.8(2)	*1680.4(1)*	492(17)	*A,B*	0.98(6)	$E2$	$19/2_1^-$	$15/2_1^-$

TABLE I. (*Continued.*)

E_x (keV)	E_γ[a] (keV)	I_{rel} (%)	Gate[b]	R_{DCO} 150°–97°	Mult. ass.	I_i^π ($\hbar$)	I_f^π ($\hbar$)
5764.2(7)	1140.1(8)	8(1)	A+B	0.39(19)[e]	$E2/M1$	$17/2_1^-$	$15/2_2^-$
	2345.9(14)	8(1)	A+B	1.05(42)	$E2/M1$	$17/2_1^-$	$15/2_1^-$
5880.8(8)	1085.8(10)	7(1)				$(17/2_2^-)$[f]	$15/2_3^-$
	1978.3(15)	4(1)				$(17/2_2^-)$	$13/2_3^-$
	2462.7(17)	9(1)				$(17/2_2^-)$	$15/2_1^-$
6059.0(6)	960.0(8)	4(1)				$(17/2_3^-)$[f]	$19/2_1^-$
	1436.2(14)	3(1)				$(17/2_3^-)$	$15/2_2^-$
	2641.7(17)	4(1)				$(17/2_3^-)$	$15/2_1^-$
	3245.8(22)	5(1)				$(17/2_3^-)$	$13/2_1^-$
6379.0(10)	1754.8(18)	3(1)			$E2$	$19/2_2^-$[f]	$15/2_2^-$
	2960.8(16)	29(1)	A+B	1.05(32)	$E2$	$19/2_2^-$	$15/2_1^-$
6457.1(10)	1415.2(11)	4(1)			$\Delta I = 1$	$17/2_4$	$(15/2_4^-)$
	1833.2(15)	7(1)	A+B	0.61(22)	$\Delta I = 1$	$17/2_4$	$15/2_2^-$
6527.2(7)	1428.4(8)	182(7)	C	0.88(10)	$E2/M1$	$21/2_1^-$	$19/2_1^-$
6903.6(7)	844.7(6)	11(1)				$(19/2_3^-)$[f]	$(17/2_3^-)$
	1139.2(9)	3(1)	A+B	0.39(19)[e]	$(E2/M1)$	$(19/2_3^-)$	$17/2_1^-$
	3484.9(22)	6(1)				$(19/2_3^-)$	$15/2_1^-$
7100.4(26)	3682.0(26)	3(1)				$(19/2_4^-)$[f]	$15/2_1^-$
7453.6(11)	996.4(8)	8(1)				$(19/2_5)$[f]	$17/2_4$
	1689.6(15)	2(1)				$(19/2_5)$	$17/2_1^-$
7603.8(9)	1076.5(6)	63(3)	C	0.66(13)	$E2/M1$	$23/2_1^-$	$21/2_1^-$
	2505.3(20)	2(1)			$E2$	$23/2_1^-$	$19/2_1^-$
7659.3(8)	755.8(6)	7(1)	A+B	0.63(43)	$E2/M1$	$(21/2_2^-)$[f]	$(19/2_3^-)$
	1280.2(13)	2(1)			$E2/M1$	$(21/2_2^-)$	$19/2_2^-$
7913.8(10)	1386.8(9)	27(3)	C	0.92(27)[e]	$E2/M1$	$23/2_2^-$[f]	$21/2_1^-$
	2814.8(19)	3(1)			$E2$	$23/2_2^-$	$19/2_1^-$
9302.2(12)	1388.8(15)	6(2)	C	0.92(27)[e]	$(\Delta I = 1)$	$(25/2_1)$	$23/2_2^-$
	1698.2(12)	6(1)	C	0.70(38)	$(\Delta I = 1)$	$(25/2_1)$	$23/2_1^-$
10301.3(16)	999.1(10)	4(1)				$(27/2_1)$[f]	$(25/2_1)$

[a]Gamma-ray energies in italic style were derived from the backed-target fraction of the data. See text for details.
[b]DCO ratios in italic style were derived from the backed-target fraction of the data. A, 1317 keV; B, 1223 keV; C, 1680 keV; D, 1370 keV; E, 1409 keV; F, 1576 keV.
[c]Assignment taken from previous work [31].
[d]Not directly observed but inferred from coincidence relationships of other transitions and previous work [31].
[e]Doublet structure.
[f](Tentative) assignment supported by yrast arguments.

606 and 274 keV into the $11/2_1^-$ level at 2539 keV, which in turn decays into the ground by two $E2$ transitions of 1223 and 1317 keV. These four transitions dominate the ^{55}Fe reference spectra shown in Fig. 2.

In particular, data taken with the thick tantalum backing, displayed in Fig. 2(a), confirm the γ-ray and level energies reported in the early work by Poletti *et al.* [26]. The γ-ray lines at 238, 385, 931, and 1370 keV seen in Fig. 2(a) define the well-known branch passing through the 931-keV $5/2_1^-$ and 2301-keV $9/2_2^-$ levels. The 1680-keV transition connects toward the 5099-keV $19/2^-$ yrast state. In Table I, all energies of γ rays emitted after the ^{55}Fe came to rest in the thick Ta backing are marked by italic notation. In fact, there is a rather abrupt transition from these "slow" transitions, depopulating levels with lifetimes $\tau > 1$ ps, to the majority of the others, which have to stem from levels with lifetimes $\tau \ll 1$ ps. This becomes most apparent when comparing the high-energy portions of the γ-ray spectra in Figs. 2(a) and 2(b), the latter based on data without tantalum backing.

The high-spin yrast scheme, marked H in Fig. 1, reaches a tentative (27/2) level at 10 301-keV excitation energy. Most of the γ-ray transitions, namely, those at 1077, 1387, 1389, 1428, and 1698 keV, have been observed previously, though in some cases listed with slightly different energies, and organized slightly differently in the respective level schemes [26–28]. In the present paper, superior $\gamma\gamma$ statistics and the observation of high-energy crossover $E2$ transitions at 2505 ($23/2_1^- \rightarrow 19/2_1^-$) and especially 2815 keV ($23/2_2^- \rightarrow 19/2_1^-$) settle this part of the level scheme. One example is the spectrum in Fig. 3(a), which is in coincidence with the $23/2_1^- \rightarrow 21/2_1^-$, 1077-keV transition. Besides the γ rays associated with the low-spin yrast scheme, L, peaks at 1428, 1698, and 999 keV appear with decreasing yields. Because of the doublet structure of the 1387- and 1389-keV transitions and the small intensities of the 1389- and 1698-keV transitions, the DCO ratios of the latter have large uncertainties while pointing at stretched dipole character. This leads to a tentative (25/2) assignment to the

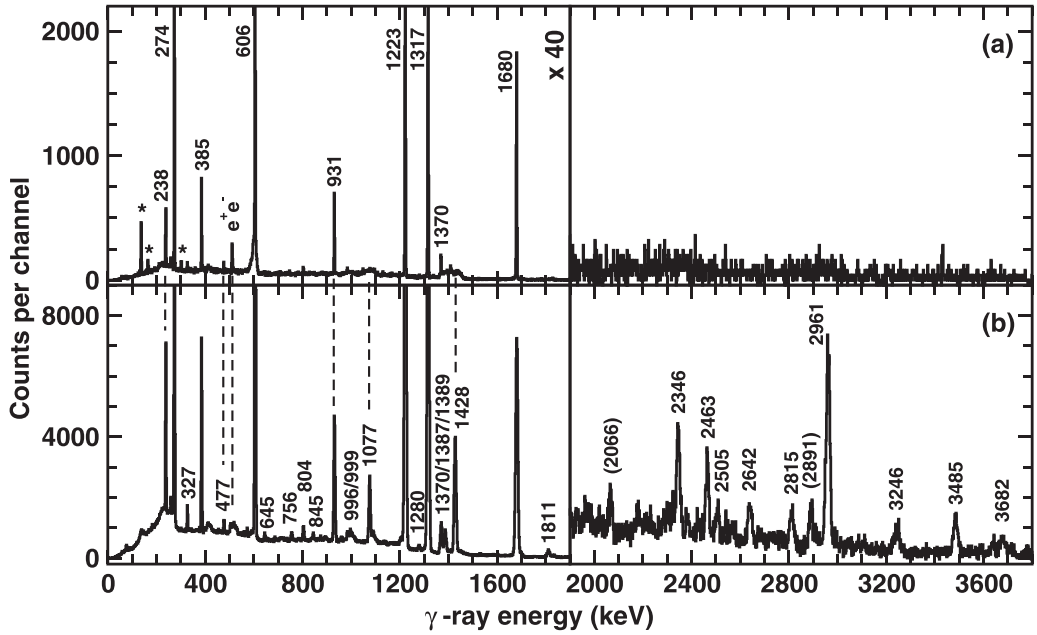

FIG. 2. Gamma-ray spectra selected for the analysis of ^{55}Fe residues according to the description in Sec. III. Both spectra are in coincidence with any of the 274-keV $13/2_1^- \rightarrow 11/2_1^-$ or 606-keV $15/2_1^- \rightarrow 13/2_1^-$ yrast transitions. The spectrum in panel (a) results from data taken with a thick Ta backing, while the spectrum in panel (b) is based on data from the main part of the experiments using the ^{28}Si targets without backing (see Sec. II for details). Energy labels are in keV, and if given in parentheses the transition could not be placed unambiguously in the ^{55}Fe level scheme. An asterisk, $*$, in panel (a) indicates background transitions from Coulomb excitation of ^{181}Ta at 136, 165, and 302 keV. The binning is 2 keV per channel. Note the significant change of y scale ($\times 40$) at 1900 keV.

9302-keV state. Yrast arguments favor (27/2) for the level at 10 301 keV.

B. The dipole structure (D)

On top of the yrare $7/2_2^-$ level at 1408 keV, a dipole structure (D) evolves. This is shown on the right-hand side of Fig. 1 and is composed of the $9/2_1^-$, $11/2_2^-$, $13/2_3^-$, $15/2_3^-$, and $(17/2_2^-)$ states at 2212, 2984, 3903, 4795, and 5881 keV excitation energy, respectively. It is characterized by relatively intense dipole transitions of 804, 772, 918, 892, and 1085 keV, accompanied by in-band quadrupole transitions of 1576, 1690, 1811, and 1978 keV. The structure is exemplified in the γ-ray spectrum in Fig. 3(d), taken in coincidence with the 804-keV $9/2_1^- \rightarrow 7/2_2^-$ transition. Besides the transitions within structure D mentioned above, there are peaks visible at, for instance, 327, 532, 601, 606, 860, and 1680 keV. These either connect into (327 and 601 keV) and are part of (606 and 1680 keV) the well-known low-spin yrast region or they belong to the intermediate region (M) discussed below (532 and 860 keV). The 477- and 1409-keV transitions connect to the yrast $5/2_1^-$ and ground state, respectively, while the peak at 411 keV in Fig. 3(d) relates to the $1/2_1^- \rightarrow 3/2_1^-$ ground-state transition. The presence of both the 385-keV $7/2_1^- \rightarrow 5/2_1^-$ as well as the 1317-keV $7/2_1^- \rightarrow 3/2_1^-$ transition determines the branch of the 92-keV $7/2_2^- \rightarrow 7/2_1^-$ connection. The transition itself is unobserved in the present paper due to attenuation of low-energy γ rays by the Microball array [42]. A minor contamination is visible at 739 keV in Fig. 3(d), which arises from the $17/2^- \rightarrow 15/2^- \rightarrow 11/2^-$ yrast cascade in the $3p2n$-evaporation channel ^{55}Co [16] based on occasional random coincidences with an additional fourth proton detected in Microball.

C. The intermediate region (M)

In earlier work [31], yrare $11/2_3^-$ and $13/2_2^-$ levels have been reported at 3072 and 3457 keV, respectively. Together with the $15/2_2^-$ state at 4624 keV, these are viewed as the intermediate region (M) in Fig. 1. Many γ rays have been and are found to connect to these three states, primarily from the low-spin (L) and dipole (D) structures. They are exemplified by the spectrum in Fig. 3(b), which is in coincidence with the 532-keV $11/2_3^- \rightarrow 11/2_1^-$ transition. The main peaks stem from coincidences with transitions belonging to the ground-state cascade (238, 327, 385, 931, 1223, and 1317 keV), while weak lines occur at, for example, 1166 and 1337 keV. Via the 385-keV $13/2_2^- \rightarrow 11/2_3^-$ transition, which is a doublet with the $7/2_1^- \rightarrow 5/2_1^-$ yrast line, the 1166-keV transition connects to the level at 4624 keV, and the 1337-keV transition connects to the level at 4795 keV, respectively. The rich information on decay branches as well as the angular correlation data (see Table I) establish spins and parities of the involved states. The R_{DCO} value of the 1811-keV transition indicates dipole character and thereby suggests the $15/2^-$ assignment to the level at 4624 keV.

D. The side structures (S)

The selectivity of the experimental setup, together with increased γ-ray efficiency at energies $E_\gamma > 2$ MeV compared with earlier studies, allows us to propose a number of hitherto unreported, weakly populated decay sequences marked S on

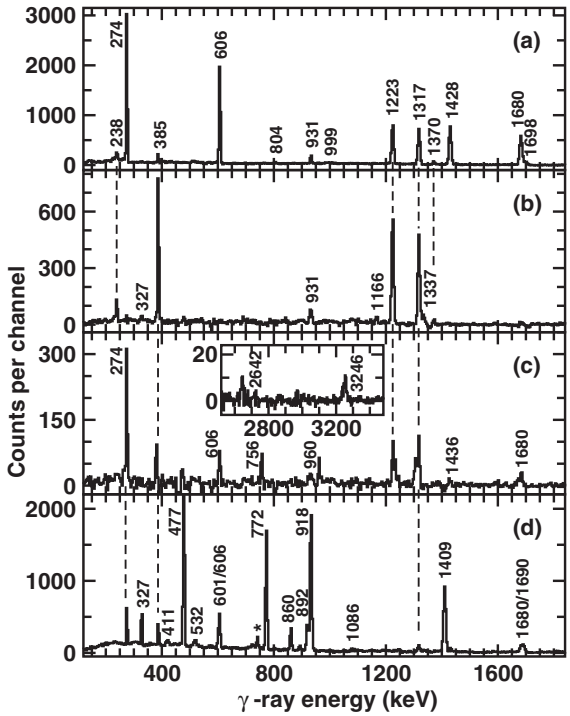

FIG. 3. Gamma-ray spectra selected for the analysis of ^{55}Fe residues according to the description in Sec. III. All spectra are based on data from the main part of the experiments using the ^{28}Si targets without Ta backing. Energy labels are in keV. The spectrum in panel (a) is in coincidence with the 1077-keV $23/2^-_1 \rightarrow 21/2^-_1$ yrast transition. The spectrum in panel (b) is in coincidence with the 532-keV $11/2^-_3 \rightarrow 11/2^-_1$ transition. The spectrum in panel (c), as well as the one shown in the inset, is in coincidence with the 845-keV transition connecting the levels at 6904 and 6059 keV. The spectrum in panel (d) is in coincidence with the 804-keV $9/2^-_1 \rightarrow 7/2^-_2$ transition. The asterisk, $*$, indicates a transition at 739 keV associated with the $17/2^- \rightarrow 15/2^- \rightarrow 11/2^-$ yrast cascade in the $3p2n$-evaporation channel ^{55}Co [16]. The binning of all spectra is 4 keV per channel.

the left-hand side of Fig. 1. A 2480-keV line is observed in coincidence with the 1317-keV ground-state transition only. The $R_{\rm DCO}$ value of the 2480-keV transition clearly indicates dipole character, i.e., in combination with yrast arguments a spin $I = 9/2$ is assigned to the 3796-keV level. A high-energy 3682-keV line is observed in coincidence with the yrast transitions up the 606-keV $15/2^-_1 \rightarrow 13/2^-_1$ one, giving rise to a state at 7100 keV, to which $I^\pi = 19/2^-$ is tentatively assigned based on yrast arguments. Transitions at 836 and 1992 keV are found to depopulate the 4293-keV state, connecting to the 3457-keV $13/2^-_2$ and 2301-keV $9/2^-_2$ levels, respectively. $R_{\rm DCO} \ll 1$ for the 836-keV line suggests spin $I = 11/2$ for the 4293-keV state.

The remaining eight levels in this structure are interconnected by at least two γ-ray transitions each. This is exemplified by the γ-ray spectrum in Fig. 3(c), which is in coincidence with the 845-keV transition connecting the 6904-keV $(19/2^-)$ and 6059-keV $(17/2^-)$ states. While a possible presence of 847-keV transitions in ^{55}Fe at lower excitation energies is commented on in Ref. [31], the coincident 2642- and 3246-keV transitions shown in the inset of Fig. 3(c), the yield ratio of the 274- and 606-keV yrast transitions, and several related coincidence spectra establish the state at 6059 keV. In Fig. 3(c), the other depopulating transitions at 960 and 1436 keV are clearly visible, as is the feeding 756-keV line. The presence of the parallel 2961-1280-keV sequence connecting the 7659-keV $(21/2^-)$ state with the yrast 3418-keV $15/2^-_1$ level, and likewise the high-energy line with 3485 keV, add further evidence for this structure; all these lines are clearly visible in Fig. 2(b). A similar level of "interconnectivity" gives confidence for the 5042-, 5764, 6457-, and 7454-keV states. Angular correlation ratios are sparse for these relatively weak structures, but combining the available $R_{\rm DCO}$ values with yrast arguments allows us to firmly assign spins (and parities) to the levels at 5764, 6379, and 6457 keV, and to propose tentative assignments for the remaining states at 5042, 6059, 6904, 7454, and 7659 keV.

V. DISCUSSION OF THE ^{55}Fe LEVEL SCHEME

The nucleus ^{55}Fe has two proton holes and one extra neutron with respect to doubly magic $N = Z = 28$ ^{56}Ni. This calls for shell-model calculations to interpret the level scheme shown in Fig. 1, which lacks any indication of regular band structures. Collective bands have been observed in ^{56}Ni [4] and in its neighboring nuclei (see, e.g., Ref. [21] and references therein), but typically at higher excitation energies and angular momenta than those accessible in the present study of ^{55}Fe.

The shell-model code ANTOINE [43,44] was used and the calculations included the full fp model space. This includes the $f_{7/2}$ orbital below and the $p_{3/2}$, $f_{5/2}$, and $p_{1/2}$ orbitals above the $N, Z = 28$ shell closure. For mass $A = 55$ nuclei it is nowadays feasible to conduct unrestricted calculations in this model space. However, this turned out to be time consuming due to the relatively large number of up to six states per spin to be assessed. Therefore, the majority of calculations employed a truncation scheme allowing for an excitation of up to six nucleons from the $0f_{7/2}$ shell into the upper fp shell ($t = 6$). Such a truncation scheme was used before, for instance, in a study of yrast structures in $A = 50$, 51, and 52 [11], or to successfully describe a rotational band in doubly magic ^{56}Ni [4]. Nevertheless, a comparison between predictions from unrestricted calculations and those using different truncation schemes ($t = 2, t = 4, t = 6, t = 8, t = 10$) was conducted at first. This was done for the main near-yrast cascade in ^{55}Fe and reassured previous findings: $t = 6$ was found to be a good compromise between computational efforts and sufficient convergence for calculated numbers. This is illustrated in Fig. 4 and exemplified in Table II. In the figure, predicted level energies change only marginally, $\Delta E_x < 10$ keV, beyond $t = 6$. Similarly, electromagnetic decay properties remain practically constant beyond $t = 6$. This justifies the present procedure, especially when putting the above trends in relation to the spread of predictions for different interactions or parametrizations.

Two common interactions were studied, GXPF1A [13] and KB3G [11]. To probe the influence of isospin breaking

TABLE II. Selected electromagnetic decay properties of states in ^{55}Fe as a function of truncation of the shell-model space, i.e., allowing $t = 2$, 4, 6, 8, 10, or any number of nucleons to be excited across the $N = Z = 28$ shell gaps. The evolution of predictions is exemplified on behalf of the KB3G interaction.

	Truncation					
Observable	$t = 2$	$t = 4$	$t = 6$	$t = 8$	$t = 10$	Full space
$B(E2; 19/2_1^- \rightarrow 15/2_1^-)$ (e^2 fm^4)	0.288	0.556	0.702	0.720	0.748	0.663
$B(M1; 15/2_1^- \rightarrow 13/2_1^-)$ (μ_N^2)	0.955	0.861	0.841	0.846	0.841	0.842
$B(E2; 7/2_1^- \rightarrow 3/2_1^-)$ (e^2 fm^4)	91.9	121	133	136	136	137
$b(7/2_1^- \rightarrow 5/2_1^-)$ (%)	21.6	14.4	12.6	12.1	12.2	12.1
$\delta(E2/M1; 7/2_1^- \rightarrow 5/2_1^-)$	−0.02	−0.03	−0.03	−0.03	−0.03	−0.03

effects, calculations based on KB3G but modified according to the prescription of Ref. [14] were performed as well, not the least because that inclusion improved the shell-model description of other nuclei close by [21,45]. For completeness, an empirical isotensor isospin-non-conserving interaction was accounted for as well [46]. This set of calculations carries the label "KB3G-ISB." During the shell-model analysis (see below) it was found that states assigned to a well-defined dipole structure based on a neutron $\nu(f_{7/2})^{-1}$ excitation were consistently predicted ≈300 keV too high in energy. An *ad hoc* solution is a corresponding 300-keV reduction of the shell gap at $N = Z = 28$, which significantly improved the theoretical description, in particular in combination with the ISB terms (see below). The corresponding calculations carry the labels "KB3G56" and "KB3G56-ISB," respectively.

Electromagnetic decay properties were probed using bare g factors and effective charges of $\varepsilon_p = 1.15e$ and $\varepsilon_n = 0.80e$ for protons and neutrons, respectively [47]. The experimental γ-ray energies were used to compute transition strengths and deduce branching and mixing ratios of the transitions, and lifetimes of the nuclear states.

The association of observed and calculated levels started from the predicted sequence of states for a given spin value. There are, however, a few consecutive states lying close in energy. In case an exchange of these provided considerably improved descriptions of both their feeding and decay pattern, the latter became the leading argument for the association of observed and calculated levels. Once the association was settled, mean level deviations (MLD) in conjunction with binding energy shifts (BES) provide an overview of the level of agreement between experiment and theory in terms of excitation energies. MLD and BES values are summarized in Table III. To better estimate the quality of the predicted wave functions one can evaluate electromagnetic decay properties.

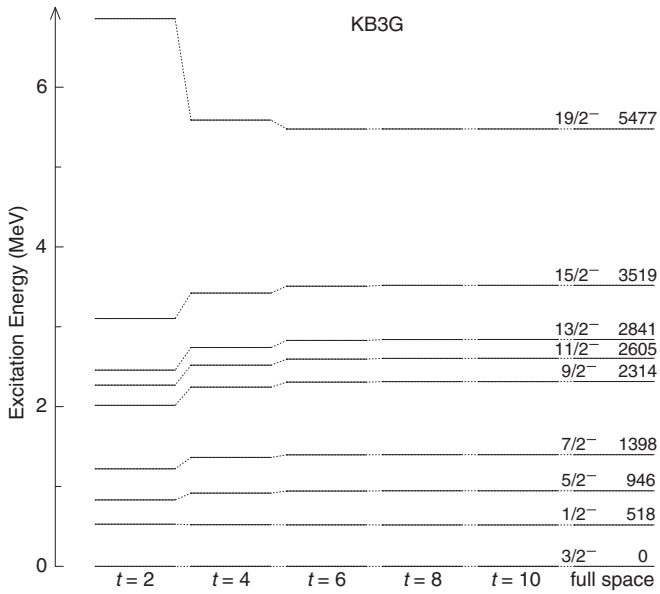

FIG. 4. Calculated level energies of the low- to medium-spin yrast sequence of ^{55}Fe as a function of truncation of the full fp model space; $t = 2$, 4, 6, 8, 10 particles are allowed to cross the shell gap at particle number $N = Z = 28$. Results of an unrestricted calculation are shown to the very right, including predicted energies in keV. The convergence of predicted level energies, reached at $t = 6$, is exemplified for the KB3G interaction.

TABLE III. Numerical assessments of the level of agreement between matched observed and calculated shell-model states in ^{55}Fe by means of mean level deviations (MLD), binding energy shifts (BES), and mean branching deviation (MBD) [48]. For a given isotope and shell-model parametrization, results are provided for strongly populated, mainly yrast states (y), and for all states (a) that allow a mapping between experiment and theory. See Table IV for details. The number of states considered is given in parentheses, (n_1, n_2), with n_1 being the number of states used for MLD and BES and n_2 for MBD, respectively.

Shell-model interaction	States	MLD (keV)	BES (keV)	MBD
GXPF1A[a]	y (20,18)	152	129	0.043
	a (31,29)	181	156	0.051
KB3G[b]	y (20,18)	199	−156	0.038
	a (31,29)	254	−183	0.049
KB3G-ISB[b]	y (20,18)	193	−41	0.029
	a (31,29)	220	−62	0.043
KB3G56[c]	y (20,18)	105	−70	0.046
	a (31,29)	160	−73	0.054
KB3G56-ISB[a]	y (20,18)	115	43	0.022
	a (31,29)	146	66	0.036

[a]Predicted $7/2_1^-$ and $7/2_2^-$ states exchanged. See text for details.
[b]Predicted $9/2_1^-$ and $9/2_2^-$ as well as $11/2_2^-$ and $11/2_3^-$ states exchanged. See text for details.
[c]Predicted $9/2_1^-$ and $9/2_2^-$ states exchanged. See text for details.

TABLE IV. Selection of experimental (Table I and [31]) and predicted branching ratios of excited states in ^{55}Fe. Energies of unobserved (n.o.) γ-ray transitions are listed in italic characters. Spin-parity labels in square brackets, $[I_i^\pi]$, represent possible theoretical assignments, which are discussed in the text. The column labeled "set" refers to the classification of states used for MLD, BES, and MBD assessments (see Table III).

E_x (keV)	Set[a]	E_γ[c] (keV)	I_i^π ($\hbar$)	I_f^π ($\hbar$)	$b_{\rm exp}$	GXPF1A	KB3G	KB3G-ISB	KB3G56	KB3G56-ISB
931	y	520	$5/2_1^-$	$1/2_1^-$	1.7(4)	2.9	3.6	3.9	3.3	3.5
		931	$5/2_1^-$	$3/2_1^-$	98.3(4)	97.1	96.4	96.1	96.7	96.5
1317	y	385	$7/2_1^-$	$5/2_1^-$	7.6(5)	11.0	12.5	10.7	11.1	9.2
		1317	$7/2_1^-$	$3/2_1^-$	92.4(5)	89.0	87.5	89.3	88.9	90.8
1408	y	92	$7/2_2^-$	$7/2_1^-$	4(1)	1	0	0	0	0
		477	$7/2_2^-$	$5/2_1^-$	63(2)	0	62	60	40	81
		1408	$7/2_2^-$	$3/2_1^-$	33(2)	99	38	40	60	19
1749[b]	a	1507	$1/2_2^-$	$1/2_1^-$	32(2)	35	41	38	38	35
		1918	$1/2_2^-$	$3/2_1^-$	68(2)	64	59	62	62	65
2051	a	*1121*	$3/2_2^-$	$5/2_1^-$	n.o.	7	7	8	7	7
		1641	$3/2_2^-$	$1/2_1^-$	77(2)	67	78	79	78	80
		2051[b]	$3/2_2^-$	$3/2_1^-$	23(3)	26	15	13	15	13
2144[b]	a	827	$5/2_2^-$	$7/2_1^-$	36(5)	43	60	61	58	59
		1213	$5/2_2^-$	$5/2_1^-$	43(5)	39	22	23	23	23
		1733	$5/2_2^-$	$1/2_1^-$	3(1)	4	3	3	3	4
		2144	$5/2_2^-$	$3/2_1^-$	18(3)	12	15	13	15	14
2212	y	804	$9/2_1^-$	$7/2_2^-$	95(2)	89	100	100	88	99
		895	$9/2_1^-$	$7/2_1^-$	3(1)	10	0	0	1	0
		1281	$9/2_1^-$	$5/2_1^-$	2(1)	1	0	0	10	1
2302	y	893	$9/2_2^-$	$7/2_2^-$	4(1)	2	0	0	62	23
		984	$9/2_2^-$	$7/2_1^-$	18(1)	12	8	7	3	6
		1370	$9/2_2^-$	$5/2_1^-$	79(2)	86	92	93	35	71
2539	y	238	$11/2_1^-$	$9/2_2^-$	6.0(3)	10.8	10.3	10.2	7.0	7.6
		327	$11/2_1^-$	$9/2_1^-$	0.9(1)	0.1	1.8	1.5	4.7	2.4
		1131	$11/2_1^-$	$7/2_2^-$	n.o.	3.5	0.1	0.1	0.6	0.4
		1223	$11/2_1^-$	$7/2_1^-$	93.1(4)	85.5	87.8	88.2	87.7	89.5
2813	y	274	$13/2_1^-$	$11/2_1^-$	98.7(3)	97.7	99.2	99.1	99.2	98.8
		512	$13/2_1^-$	$9/2_2^-$	0.5(1)	2.2	0.7	0.8	0.7	0.6
		601	$13/2_1^-$	$9/2_1^-$	0.7(1)	0.1	0.2	0.2	0.1	0.6
2984	y	*171*	$11/2_2^-$	$13/2_1^-$	n.o.	0	0	0	0	0
		445	$11/2_2^-$	$11/2_1^-$	13(2)	0	0	0	14	14
		682	$11/2_2^-$	$9/2_2^-$	n.o.	2	1	1	13	3
		772	$11/2_2^-$	$9/2_1^-$	59(3)	63	67	67	44	56
		1576	$11/2_2^-$	$7/2_2^-$	19(2)	34	31	31	28	27
		1668	$11/2_2^-$	$7/2_1^-$	9(2)	1	1	1	0	0
3072	y	258	$11/2_3^-$	$13/2_1^-$	14(3)	24	9	7	9	7
		532	$11/2_3^-$	$11/2_1^-$	42(5)	72	66	66	51	48
		770	$11/2_3^-$	$9/2_2^-$	14(3)	0	5	6	16	4
		860	$11/2_3^-$	$9/2_1^-$	18(3)	2	7	8	2	18
		1663	$11/2_3^-$	$7/2_2^-$	7(2)	0	2	3	7	8
		1756	$11/2_3^-$	$7/2_1^-$	5(2)	2	11	11	14	14
3418	y	*346*	$15/2_1^-$	$11/2_3^-$	n.o.	0.0	0.0	0.0	0.0	0.0
		434	$15/2_1^-$	$11/2_2^-$	n.o.	0.0	0.0	0.0	0.0	0.0
		606	$15/2_1^-$	$13/2_1^-$	98.6(2)	98.9	99.2	99.1	99.1	99.0
		879	$15/2_1^-$	$11/2_1^-$	1.4(2)	1.1	0.8	0.8	0.9	1.0
3457	y	385	$13/2_2^-$	$11/2_3^-$	26(4)	37	14	13	14	14
		473	$13/2_2^-$	$11/2_2^-$	10(2)	2	2	2	2	2
		498	$13/2_2^-$	$9/2_3^-$	n.o.	0	0	0	0	0
		645	$13/2_2^-$	$13/2_1^-$	4(2)	3	1	1	4	3
		918	$13/2_2^-$	$11/2_1^-$	55(6)	40	79	81	75	78
		1157	$13/2_2^-$	$9/2_2^-$	3(1)	12	3	2	1	4
		1245	$13/2_2^-$	$9/2_1^-$	3(1)	7	1	1	5	0
3796	?	2480	$[9/2_5^-]$	$7/2_1^-$	100	21	11	10	8	16

TABLE IV. (*Continued*.)

E_x (keV)	Set[a]	E_γ[c] (keV)	I_i^π ($\hbar$)	I_f^π ($\hbar$)	$b_{\rm exp}$	GXPF1A	KB3G	KB3G-ISB	KB3G56	KB3G56-ISB
3903	y	*446*	$13/2_3^-$	$13/2_2^-$	n.o.	8	0	0	7	7
		485	$13/2_3^-$	$15/2_1^-$	n.o.	0	3	0	0	0
		831	$13/2_3^-$	$11/2_3^-$	n.o.	7	3	2	0	0
		918	$13/2_3^-$	$11/2_2^-$	63(5)	40	33	33	40	40
		1090	$13/2_3^-$	$13/2_1^-$	15(3)	20	38	38	37	34
		1364	$13/2_3^-$	$11/2_1^-$	n.o.	2	1	3	1	1
		1601	$13/2_3^-$	$9/2_2^-$	n.o.	1	4	5	7	0
		1690	$13/2_3^-$	$9/2_1^-$	22(3)	22	18	18	9	18
4293	?	836	$[11/2_4^-]$	$13/2_2^-$	70(10)	2	1	3	1	1
		1992	$[11/2_4^-]$	$9/2_2^-$	30(10)	6	56	14	39	2
4624	y	*721*	$15/2_2^-$	$13/2_3^-$	n.o.	9	0	0	2	2
		1166	$15/2_2^-$	$13/2_2^-$	28(2)	15	59	56	47	44
		1206	$15/2_2^-$	$15/2_1^-$	28(2)	28	8	8	12	12
		1640	$15/2_2^-$	$11/2_3^-$	n.o.	7	0	0	1	1
		1811	$15/2_2^-$	$13/2_1^-$	45(3)	39	32	35	38	40
4795	y	892	$15/2_3^-$	$13/2_3^-$	16(4)	6	20	19	14	14
		1337	$15/2_3^-$	$13/2_2^-$	52(8)	75	19	20	40	38
		1377	$15/2_3^-$	$15/2_1^-$	19(7)	0	31	31	26	27
		1811	$15/2_3^-$	$11/2_2^-$	16(5)	9	21	21	13	13
		1982	$15/2_3^-$	$13/2_1^-$	n.o.	9	8	8	5	5
5042	?	*1139*	$[15/2_4^-]$	$13/2_3^-$	n.o.	15	13	9	4	0
		1585	$[15/2_4^-]$	$13/2_2^-$	27(9)	7	7	6	8	0
		1624	$[15/2_4^-]$	$15/2_1^-$	n.o.	20	52	44	49	7
		2229	$[15/2_4^-]$	$11/2_1^-$	n.o.	6	3	7	7	78
		2502	$[15/2_4^-]$	$11/2_1^-$	73(9)	47	25	32	31	13
5099	y	*304*	$19/2_1^-$	$15/2_3^-$	n.o.	0.0	0.1	0.1	0.1	0.1
		475	$19/2_1^-$	$15/2_2^-$	n.o.	0.2	0.1	0.1	0.1	0.1
		1680	$19/2_1^-$	$15/2_1^-$	100	99.7	99.8	99.8	99.8	99.8
5764	y	*665*	$17/2_1^-$	$19/2_1^-$	n.o.	0	0	0	0	1
		969	$17/2_1^-$	$15/2_3^-$	n.o.	6	1	1	3	3
		1140	$17/2_1^-$	$15/2_2^-$	50(6)	20	50	48	46	44
		2307	$17/2_1^-$	$13/2_2^-$	n.o.	9	4	4	4	4
		2346	$17/2_1^-$	$15/2_1^-$	50(6)	61	37	39	40	43
		2951	$17/2_1^-$	$13/2_1^-$	n.o.	4	6	6	6	6
5881	a	*782*	$[17/2_2^-]$	$19/2_1^-$	n.o.	4	5	5	3	3
		1086	$[17/2_2^-]$	$15/2_3^-$	35(6)	22	51	51	41	38
		1978	$[17/2_2^-]$	$13/2_3^-$	20(6)	17	17	15	20	20
		2463	$[17/2_2^-]$	$15/2_1^-$	45(7)	47	24	25	23	26
6059	a	*178*	$[17/2_3^-]$	$17/2_2^-$	n.o.	0	0	0	0	0
		960	$[17/2_3^-]$	$19/2_1^-$	25(8)	10	32	31	30	28
		1017	$[17/2_3^-]$	$[15/2_4^-]$	n.o.	0	11	8	7	5
		1436	$[17/2_3^-]$	$15/2_2^-$	19(8)	2	10	11	11	12
		2642	$[17/2_3^-]$	$15/2_1^-$	25(8)	34	5	6	5	7
		3246	$[17/2_3^-]$	$13/2_1^-$	31(9)	51	39	39	41	40
6379	a	*498*	$19/2_2^-$	$[17/2_2^-]$	n.o.	3	11	11	9	9
		1280	$19/2_2^-$	$19/2_1^-$	n.o.	11	13	11	11	9
		1584	$19/2_2^-$	$15/2_3^-$	n.o.	3	26	25	20	20
		1755	$19/2_2^-$	$15/2_2^-$	9(3)	10	1	1	4	4
		2961	$19/2_2^-$	$15/2_1^-$	91(3)	72	44	47	51	56
6457	?	*1358*	$[17/2_4^-]$	$19/2_1^-$	n.o.	6	2	0	30	25
		1415	$[17/2_4^-]$	$[15/2_4^-]$	36(9)	0	15	6	3	27
		1833	$[17/2_4^-]$	$15/2_2^-$	64(9)	14	1	2	6	6
		3039	$[17/2_4^-]$	$15/2_1^-$	n.o.	69	43	52	0	2
6527	y	*646*	$21/2_1^-$	$[17/2_2^-]$	n.o.	0	0	0	0	0
		763	$21/2_1^-$	$17/2_1^-$	n.o.	0	0	0	0	0
		1428	$21/2_1^-$	$19/2_1^-$	100	100	100	100	100	100

TABLE IV. (*Continued.*)

E_x (keV)	Set[a]	E_γ[c] (keV)	I_i^π ($\hbar$)	I_f^π ($\hbar$)	$b_{\exp}$	GXPF1A	KB3G	KB3G-ISB	KB3G56	KB3G56-ISB
6904	a	845	$[19/2_4^-]$	$[17/2_3^-]$	55(7)	26	20	22	15	13
		1140	$[19/2_4^-]$	$17/2_1^-$	15(6)	9	5	5	5	6
		1805	$[19/2_4^-]$	$19/2_1^-$	n.o.	1	14	16	16	20
		3485	$[19/2_4^-]$	$15/2_1^-$	30(6)	45	55	50	60	55
7100	?	3682	$[19/2_5^-]$	$15/2_1^-$	100	22	79	48	39	38
7454	?		$(19/2_5)$			cannot be assigned				
7604	y	1077	$23/2_1^-$	$21/2_1^-$	97(2)	31	59	90	59	92
		1225	$23/2_1^-$	$19/2_2^-$	n.o.	3	2	0	2	0
		2505	$23/2_1^-$	$19/2_1^-$	3(2)	65	39	10	39	8
7659	a	756	$[21/2_3^-]$	$[19/2_4^-]$	78(11)	3	15	17	15	17
		1132	$[21/2_3^-]$	$21/2_1^-$	n.o.	14	10	14	15	24
		1202	$[21/2_3^-]$	$[17/2_4^-]$	n.o.	1	1	1	0	0
		1280	$[21/2_3^-]$	$19/2_2^-$	22(11)	51	37	28	27	14
		1778	$[21/2_3^-]$	$[17/2_2^-]$	n.o.	8	24	22	23	19
7914	a	1387	$23/2_2^-$	$21/2_1^-$	90(4)	98	99	94	99	80
		1535	$23/2_2^-$	$19/2_2^-$	n.o.	1	0	3	0	7
		2815	$23/2_2^-$	$19/2_1^-$	10(4)	1	1	2	1	12
9302	a	1389	$[25/2_1^-]$	$23/2_2^-$	50(8)	95	93	32	93	17
		1698	$[25/2_1^-]$	$23/2_1^-$	50(8)	1	5	67	5	82
		2775	$[25/2_1^-]$	$21/2_1^-$	n.o.	2	1	1	1	1
10301	a	999	$[27/2_1^-]$	$[25/2_1^-]$	100	48	78	82	78	83
		2387	$[27/2_1^-]$	$23/2_2^-$	n.o.	0	1	9	1	12
		2697	$[27/2_1^-]$	$23/2_1^-$	n.o.	52	21	9	21	5

[a]y, near-yrast structure; a, all mapped states; ?, questionable.
[b]Not observed in the present experiment.
[c]The following calculated levels were exchanged: GXPF1A, $7/2_1^-$ and $7/2_2^-$; KB3G, $9/2_1^-$ and $9/2_2^-$, $11/2_2^-$ and $11/2_3^-$, $11/2_4^-$ and $11/2_5^-$, and $19/2_5^-$ and $19/2_6^-$; KB3G-ISB, $9/2_1^-$ and $9/2_2^-$, and $11/2_2^-$ and $11/2_3^-$; KB3G56, $9/2_1^-$ and $9/2_2^-$; KB3G56-ISB, $7/2_1^-$ and $7/2_2^-$, and $9/2_4^-$ and $9/2_5^-$.

These gave rise to comparisons between observed and calculated branching ratios in Table IV and a few lifetimes in Table V. To assess the level of agreement of these decay properties, mean branching deviations (MBD) [48] are provided in Table III.

Starting with the plain GXPF1A and KB3G interactions, the numbers in Table III indicate that both provide a good description of the energies and decay patterns of the observed levels. GXPF1A performs somewhat better for the energies (MLD), and KB3G performs somewhat better for branching ratios (MBD). For the yrast sequence (see Table IV), GXPF1A has problems catching the ratio between the 1409-keV $7/2_2^- \rightarrow 3/2_1^-$ and 477-keV $7/2_2^- \rightarrow 5/2_1^-$ transitions and the decay pattern of the 7604-keV $23/2_1^-$ level. Similar to a shell-model study of ^{53}Mn and ^{54}Fe [21], GXPF1A calls for relatively large positive BES, opposite to similarly large negative BES for KB3G. A BES approaching zero is achieved for the KB3G-ISB attempt, though the corresponding MLD remains similarly high for the yrast states, denoted y in Tables III and IV. However, a significant improvement is observed for the MBD value, decreasing from 0.038 (KB3G) to 0.029 (KB3G-ISB) for the yrast states, with the main difference arising from the considerably improved description of the 7604-keV $23/2_1^-$ level.

Interesting facets of the ^{55}Fe level scheme are the energetically nearly degenerate first two $7/2^-$ states at 1317 and 1408 keV, as well as the first two $9/2^-$ states at 2212 and 2301 keV. The $7/2_1^-$ and $9/2_2^-$ states belong to the main low-spin part, L, while the $7/2_2^-$ and the $9/2_1^-$ states form the beginning of the strongly coupled dipole structure, D, as illustrated in Fig. 1. In the region around ^{56}Ni, such dipole structures are typically based on unpaired $f_{7/2}$ holes. The cranked Nilsson-Strutinsky approach associates these with configurations with one hole in a high-j shell, here $f_{7/2}$, which generate signature degeneracy at deformation $\gamma > -30^\circ$ (see, for instance, the discussion of the dipole bands observed in ^{54}Fe in Ref. [21]). In fact, evaluating the main partitions of the predicted shell-model wave functions for states in ^{55}Fe, one can easily identify a sequence built upon a neutron $\nu(f_{7/2})^{-1}$ hole configuration; the calculated states mapped onto the experimental $7/2_2^-$, $9/2_1^-$, $11/2_2^-$, $13/2_3^-$, $15/2_3^-$, and $17/2_2^-$ states at 1408, 2212, 2984, 3903, 4795, and 5881 keV are composed of close to 50% partitions of the type $\pi(f_{7/2})^{-2}_{0,2} \times \nu(f_{7/2})^{-1} \times \nu(fp)^2_{0-4}$ for all interactions and parametrizations considered. The assignment of these states is nicely corroborated by the corresponding branching ratios listed in Table IV.

Further evaluation of leading wave-function partitions leads to the mapping of calculated states onto the $3/2_1^-$ ground state and the $5/2_2^-$, $7/2_1^-$, $(9/2_3^-)$, $11/2_1^-$, $13/2_1^-$, and $15/2_1^-$ states found at 2144, 1317, (unknown), 2539, 2813, and 3418 keV. These are of the type $\pi(f_{7/2})^{-2}_{0,2,4,6} \times \nu(p_{3/2})$. In turn, the $5/2_1^-$, $(7/2_4^-)$, $9/2_2^-$, $(11/2_4^-)$, $13/2_2^-$, $15/2_2^-$, and

TABLE V. Overview of experimental [31] and predicted lifetimes of near-yrast states in ^{55}Fe.

E_x (keV)	I_i^π ($\hbar$)	$\tau_{\rm exp}$ (ps)	GXPF1A (ps)	KB3G (ps)	KB3G-ISB (ps)	KB3G56 (ps)	KB3G56-ISB (ps)
411	$1/2_1^-$	$9(^{9}_{4})$	1.6	0.90	0.95	0.96	1.0
931	$5/2_1^-$	12(4)	4.9	7.6	8.0	6.5	6.8
1317	$7/2_1^-$	$3(^{2}_{1})$	1.1	1.3	1.3	1.3	1.2
1408	$7/2_2^-$	54.7(25)	7.9	146	137	113	141
1918[a]	$1/2_2^-$	0.017(6)	0.039	0.026	0.025	0.026	0.025
2051	$3/2_2^-$	0.011(3)	0.028	0.027	0.029	0.029	0.031
2144[a]	$5/2_2^-$	$0.055(^{16}_{12})$	0.064	0.047	0.050	0.048	0.052
2212	$9/2_1^-$	1.1(3)	0.87	0.37	0.37	0.58	0.39
2301	$9/2_2^-$	$0.9(^{7}_{3})$	0.41	1.1	1.1	0.46	0.81
2539	$11/2_1^-$	13.4(19)	2.8	3.2	3.2	3.0	3.1
2813	$13/2_1^-$	14(3)	25.6	9.2	9.6	9.6	10.0
2984	$11/2_2^-$		0.27	0.31	0.31	0.30	0.28
3072	$11/2_3^-$		0.81	0.32	0.31	0.39	0.38
3418	$15/2_1^-$	0.10(3)	0.32	0.30	0.31	0.31	0.33
3457	$13/2_2^-$		1.0	0.32	0.28	0.36	0.33
3903	$13/2_3^-$		0.091	0.13	0.13	0.082	0.079
4624	$15/2_2^-$		0.048	0.031	0.031	0.032	0.031
4795	$15/2_3^-$		0.040	0.058	0.057	0.042	0.041
5099	$19/2_1^-$	32.3(12)	13.4	85.4	85.0	73.3	73.3
5764	$17/2_1^-$		0.023	0.033	0.032	0.033	0.032
5881	$17/2_2^-$		0.027	0.049	0.048	0.039	0.039
6527	$21/2_1^-$	<1	0.045	0.040	0.040	0.041	0.041
7604	$23/2_1^-$		0.29	0.21	0.055	0.20	0.047
7914	$23/2_2^-$		0.024	0.022	0.066	0.023	0.13
9302	$25/2_1^-$		0.021	0.020	0.014	0.020	0.013
10301	$27/2_1^-$		0.080	0.083	0.088	0.082	0.089

[a]Not observed in the present experiment.

$17/2_1^-$ at 931, (unknown), 2301, (unknown), 3457, 4624, and 5764 keV are mapped onto states with leading $\pi(f_{7/2})^{-2}_{0,2,4,6} \times \nu(f_{5/2})$ partitions. The same picture of a split of most of the states with $I \leqslant 17/2$, negative parity, and $E_x \leqslant 6$ MeV into these three categories arises when considering occupation numbers. Figure 5 exemplifies these with the KB3G predictions. Figures 5(a) and 5(b) represent states mapped onto the $\nu(p_{3/2})$ and $\nu(f_{5/2})$ configurations, respectively.

For $\nu(p_{3/2})$ (solid green) and $\nu(f_{5/2})$ (long-dashed cyan) in Figs. 5(a) and 5(b), respectively, $n \approx 1.0$ is seen, on top of $n \approx 0.5$ particles being excited across the $N = 28$ gap as well $n \approx 0.5$ particles across the $Z = 28$ gap. The latter can easily be recognized in Figs. 5(a) and 5(b) by the almost horizontal lines for $\nu(f_{7/2})^{-1}$ (blue long-dashed line, $n \approx -0.5$) and $\pi(f_{7/2})^{-1}$ (red dashed line, $n \approx -2.5$). In turn, Fig. 5(c) shows the occupation numbers calculated for the states associated with a leading $\nu(f_{7/2})^{-1}$ partition. Consequently, and in agreement with the interpretation, $n \approx -1.3$ for holes in the $\nu(f_{7/2})$ orbital, and on average $n \approx 2.3$ for the upper fp neutron shell occupation (solid black line). Note that all lines shown in Fig. 5 indicate essentially constant occupation numbers along the three structures discussed. Finally, the yrast $1/2_1^-$ level observed at 411 keV finds its theoretical counterpart in an approximately 25% $\pi(f_{7/2})^{-2}_0 \times \nu(p_{1/2})$ partition of the calculated yrast $1/2^-$ state. The theoretical counterpart of the $11/2_3$ state at 3072 keV located in part M of Fig. 1 is a mixture of all three types of excitations described earlier. Occupation numbers taken from the KB3G-ISB parametrization are merely identical to those of KB3G. Interestingly, the effect of the *ad hoc* adjustment of the size of the shell gap (KB3G56-ISB) leads to rather small changes of occupation numbers. On average, only an additional $\Delta n \approx 0.07$–0.09 particles are predicted to be excited across the $N = 28$ and $Z = 28$ shell gaps in any of the three panels, i.e., by and large independent of leading partition and spin.

Based on the above classification scheme of excited states in ^{55}Fe, Fig. 6 presents comparisons of observed and calculated level energies for the three different subsets of states, as well as the high-spin yrast region, $I \geqslant 19/2$. For each subset, the KB3G, KB3G-ISB, and KB3G56-ISB results are shown left from the experimental energy, and the GXPF1A predictions to their right. The $\nu(p_{3/2})$ and $\nu(f_{5/2})$ subsets are very well described up to 4-MeV excitation energy. Here, the KB3G-ISB and KB3G56-ISB modifications yield only slight improvements. With a few exceptions, GXPF1A underpredicts the level energies somewhat, in particular the $\nu(f_{7/2})^{-1}$ and high-spin subsets. This is the reason for the positive BES $= +129$ keV. KB3G behaves opposite: BES $= -156$ keV (see Table III). Moreover, even including the ISB correction, the $\nu(f_{7/2})^{-1}$ subset is consistently overpredicted by 200–300 keV. Because of this subset's shell-model identity, this mismatch can be accounted for by decreasing the shell gap at $N = Z = 28$ by 300 keV, which is represented by the KB3G56-ISB columns. Not only does this *ad hoc* correction

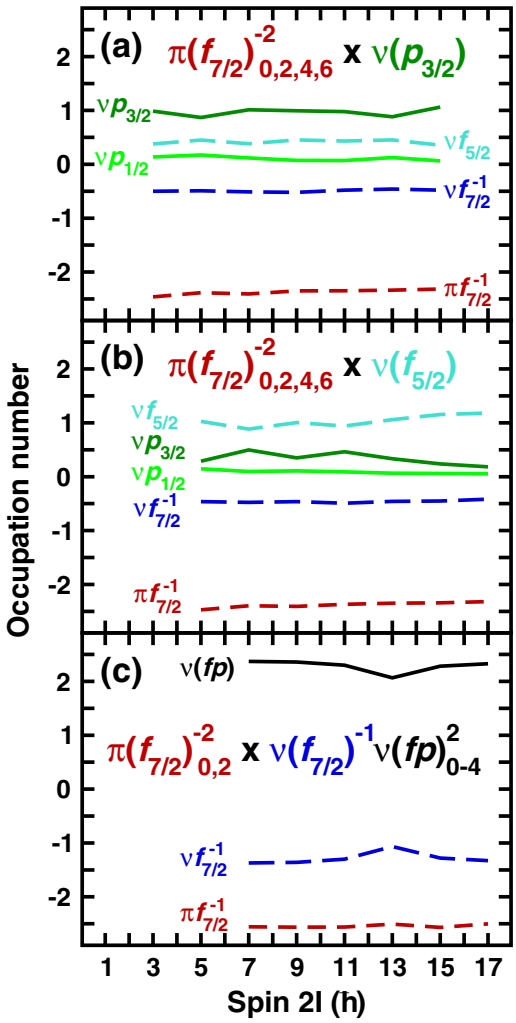

FIG. 5. Occupation numbers relative to ^{56}Ni, i.e., the number of holes in case of $f_{7/2}$ orbitals, and the number of particles for the upper-fp-shell orbitals. The three panels are labeled with three different leading wave-function partitions (≈40–50 %) identified in the level scheme of ^{55}Fe: (a) $\pi(f_{7/2})^{-2}_{0,2,4,6} \times \nu(p_{3/2})$, I = 3/2-15/2; (b) $\pi(f_{7/2})^{-2}_{0,2,4,6} \times \nu(f_{5/2})$, I = 5/2-17/2; (c) $\pi(f_{7/2})^{-2}_{0,2} \times \nu(f_{7/2})^{-1}\nu(fp)^{2}_{0-4}$, I = 7/2-17/2. The numbers are from shell-model calculations in the fp model space using the KB3G interaction (see Sec. V). Solid lines represent the $\nu p_{3/2}$ (dark green) and $\nu p_{1/2}$ (green) orbital occupation numbers, and in panel (c) the summed occupation numbers of all upper-fp neutron orbitals are labeled $\nu(fp)$ (black). Long-dashed lines are used for the $\nu f_{5/2}$ (cyan) occupation numbers and number of holes in $\nu f^{-1}_{7/2}$ (blue). The number of holes in $\pi f^{-1}_{7/2}$ (red) are shown by a dashed line.

considerably improve the overall comparative energetics, it also does it for the decay pattern of several yrast levels. With MLD = 115 keV, BES = +43 keV, and particularly MBD = 0.022, excellent agreement between experiment and KB3G56-ISB predictions is obtained.

The lifetime predictions summarized in Table V are in very good agreement with experimental values and related observations. For the 5099-keV $19/2^-$ state, τ = 32.3(12) ps [31]; here, the predictions range from 13 to 85 ps, i.e., they lie within a factor of 3. The lifetimes of all states above that level are predicted in the sub-ps regime, consistent with nonobservation at rest of any γ-ray line depopulating levels on top of that 5099-keV state in Fig. 2(a). The lifetime of the 2813-keV $13/2^-$ state, τ = 14(3) ps, is similarly well described. Because of its main, ps-delayed feeding pattern, one may question the experimental value of the 2539-keV state, while the lifetimes of the low-spin yrare $5/2^-_2$, $3/2^-_2$, are $1/2^-_2$ are very well described. The prediction of the lifetime of the 1408-keV $7/2^-_2$ state, i.e., the basis of the $\nu(f_{7/2})^{-1}$ dipole structure, relates in essence to single-particle/hole transitions and is thus very sensitive to various small partitions enabling additional $M1$ or $E2$ overlap with the wave functions of the few lower lying states with different intrinsic structure. This explains the spread of calculated values between ≈10 ps (GXPF1A) and ≈140 ps (KB3G), though they encompass the measured τ = 54.7(25) ps.

One reason for the remaining energy discrepancies at high spin might be the influence of partitions engaging excitations into the $g_{9/2}$ intruder orbital. In fact, $g_{9/2}$ single-particle states are known at E_x = 3701 keV in N = 29 ^{57}Ni [17] and possibly at 3510(25) keV in Z = 29 ^{57}Cu [49]. There exist $9/2^+$ states at 3041 keV in Z = 29 ^{59}Cu [50] and at 3707 keV in N = 29 ^{53}Cr [51]. In ^{55}Fe, an I = 9/2 state at 3796 keV is newly observed. For the energetically reasonable $9/2^-_{4,5,6}$ states, none of the present shell-model calculations predicts a decay that (almost) exclusively proceeds to the yrast $7/2^-$ 1317-keV state (see Table IV). Therefore, and because all N, Z = $299/2^+$ states mentioned earlier are known to decay predominantly by a stretched $9/2^+ \rightarrow 7/2^-$ $E1$ transition, the level at 3796 keV is a prime candidate for the neutron $\nu(g_{9/2})$ single-particle state in ^{55}Fe.

With ≈40 %, the leading partition predicted for the yrast $19/2^-$ state, experimentally observed at 5099 keV, is the fully aligned three-hole $[\pi(f_{7/2})^{-2}_6 \times \nu(f_{7/2})^{-1}]_{19/2}$ configuration. It benefits from a strongly attractive $[\pi(f_{7/2})^{-1} \times \nu(f_{7/2})^{-1}]_7$ two-body matrix element, which also gives rise to the $19/2^-$ spin-gap isomers in the mass A = 53 mirror nuclei ^{53}Co and ^{53}Fe. The $19/2^-$ state in ^{55}Fe bares a resemblance to this isomeric character (see Table V and lifetime discussion above), because its leading partition cannot easily connect via $E2$ matrix elements to the leading partitions of any of the lower lying $15/2^-$ states.

The high-spin states on top of the $19/2^-$ state are based on breaking the neutron pair in the upper fp shell and coupling these two neutrons' spins in various combinations to the underlying main partition of the $19/2^-$ state. For example, two relatively closely lying $23/2^-$ states are observed and predicted, with the yrast state calculated to be composed of ≈40 % of $[\pi(f_{7/2})^{-2}_6 \times \nu(f_{7/2})^{-1} \times \nu(p_{3/2})^2_2]_{23/2}$, and the yrare state ≈50 % of $\{\pi(f_{7/2})^{-2}_6 \times \nu(f_{7/2})^{-1} \times [\nu(p_{3/2})\nu(f_{5/2})]_2\}_{23/2}$. The wave functions of the yrast $25/2^-$ and $27/2^-$ states, anticipated to match the observed states at 9302 and 10 301 keV (see decay pattern, Table IV), are predicted to be composed of partitions of ≈60 %$\{\pi(f_{7/2})^{-2}_6 \times \nu(f_{7/2})^{-1} \times [\nu(p_{3/2})\nu(f_{5/2})]_3\}_{25/2}$ and ≈65 %$\{\pi(f_{7/2})^{-2}_6 \times \nu(f_{7/2})^{-1} \times [\nu(p_{3/2})\nu(f_{5/2})]_4\}_{27/2}$, respectively. The discrepancy of the predicted energy of the $25/2^-$ state may

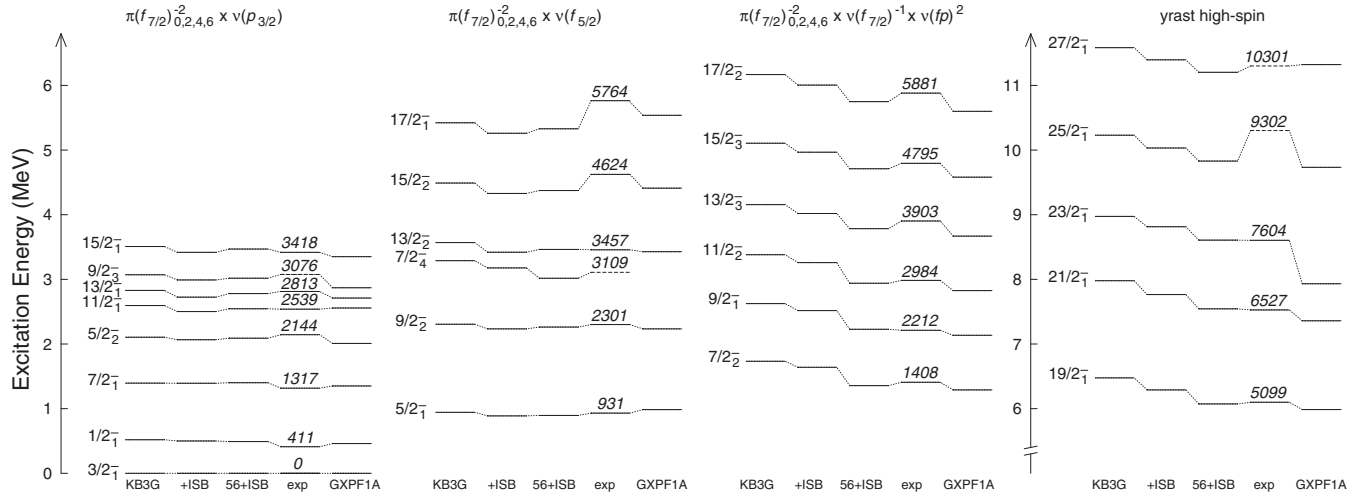

FIG. 6. Comparison of calculated level energies with experimental ones for different subsets of states in ^{55}Fe. They are ordered according to predicted leading components of the wave functions as shown on top of each subpanel, as well as the yrast high-spin states on the right-hand side. Experimental (exp) levels are labeled by their energy in keV. The index, $i = 1, 2, 3, 4$ on the spin-parity value corresponds to the ith experimental state of a given spin. Tentative levels are dashed. For each subset, the predictions of the GXPF1A and KB3G interactions are presented, the latter also including isospin-breaking terms (+ISB) and an adjustment of the size of the $N = Z = 28$ gap. See text for details.

thus be traced to two-body matrix elements engaging $[\nu(p_{3/2})\nu(f_{5/2})]_3$ couplings, though a more comprehensive high-spin level scheme with firm spin and parity assignments is required prior to any more detailed assessment.

Finally, the 6059-, 6904-, and 7659-keV states of structure S in Fig. 1 are reasonably well described by the calculated $17/2^-_3$, $19/2^-_4$, and $21/2^-_3$ levels. At variance, reasonably matching calculated states remain unidentified for the experimental levels at 4292, 5042, 6457, 7100, and 7454 keV. They correspond to the fourth or fifth non-yrast state of a given spin value.

VI. PREDICTED NEAR-YRAST STRUCTURE OF ^{55}Cu

An in-beam γ-ray study of ^{55}Cu via stable-beam induced fusion evaporation is unlikely to succeed because of tiny absolute but, more importantly, negligible relative production cross sections for ^{28}Si(^{32}S, $p4n$)^{55}Cu or ^{24}Mg(^{36}Ar, $p4n$)^{55}Cu, to name but a few. However, and despite having a proton-unbound ground state [31,52], in-beam spectroscopy of ^{55}Cu appears to be in experimental reach, since one- or two-neutron removal reactions from fast, secondary radioactive beams entered the region around ^{56}Ni about a decade ago [22–24,53–57]. By taking advantage of the excellent agreement of experimental and calculated (here the KB3G56-ISB interaction) level energies and decay pattern of the near-yrast structure of the $T_z = +3/2$ nucleus ^{55}Fe, in the following predictions are made for its $T_z = -3/2$ mirror partner ^{55}Cu.

The predictions are summarized in Fig. 7. Figure 7(a) shows the calculated energy levels for ^{55}Fe and ^{55}Cu. They are split into three columns, which reflect essentially the same subsets of levels as Fig. 6. For completeness, the yrast $1/2^-$ and $19/2^-$ yrast states are included in the left column of Fig. 7(a), which otherwise is composed of levels with the unpaired nucleon placed in the $p_{3/2}$ orbital. Mirror energy differences (MEDs) are predicted marginal for the $1/2^-_1$, $7/2^-_2$, and $19/2^-_1$ levels, but they increase to $\approx +100$ keV for the $11/2^-_1$ to $15/2^-_1$ yrast states.

For states built upon configurations with the unpaired nucleon placed in the $f_{5/2}$ orbital, rather large, positive MEDs are predicted. These are illustrated in the middle column of Fig. 7(a) and range from MED $= +200$ keV for the $5/2^-_1$ level to $+360$ keV for the $17/2^-_1$ state. Such values may appear large at first sight, but they are comparable with experimental numbers for the $A = 57$, $T_z = \pm 1/2$ pair: The $5/2^-$ (single-particle) levels are observed at 769 keV in ^{57}Ni and at 1028 keV in ^{57}Cu [16,17,49], which leads to MED$_{\rm exp} = +259$ keV.

The isospin breaking spin-orbit term, $V_{\ell s}$, changes single-particle energies for protons and neutrons in opposite direction for the spin-orbit partners $f_{5/2}$ and $f_{7/2}$ [14,15]. Consequently, for the $f^{-1}_{7/2}$ sequence shown on the right side of Fig. 7(a), typically negative values, MED $= -100$ keV, are predicted. While the two lowest $7/2^-$ states in ^{55}Fe are almost degenerate, both in experiment and theory, the $7/2^-_1$ state based on the $\pi(f_{7/2})^{-1}$ configuration in ^{55}Cu is predicted yrast by more than 150 keV compared with the $7/2^-_2$ state representing the $\nu(f_{7/2})^{-2}_2 \times \pi(p_{3/2})$ configuration. Furthermore, the hindered electromagnetic decay of the $7/2^-_1$ state implies that it resembles a 1–2-ns isomer.

Using the calculated energies of Fig. 7(a) and the experimentally known counterparts for ^{55}Fe, it is possible to better estimate experimental energies for ^{55}Cu. This was done for the proposed decay schemes shown in Figs. 7(b) and 7(c). For example, the $1/2^-_1$ state in ^{55}Fe is observed at 411 keV and predicted at 491 keV. The $1/2^-_1$ state in ^{55}Cu is predicted at 498 keV, i.e., it is expected to lie at $(411 - 491 + 498)$ keV $= 418$ keV. Since transition energies are affected, predicted branching ratios are subject to change, though the overall line of discussion below remains essentially the same if the originally calculated level energies were used instead.

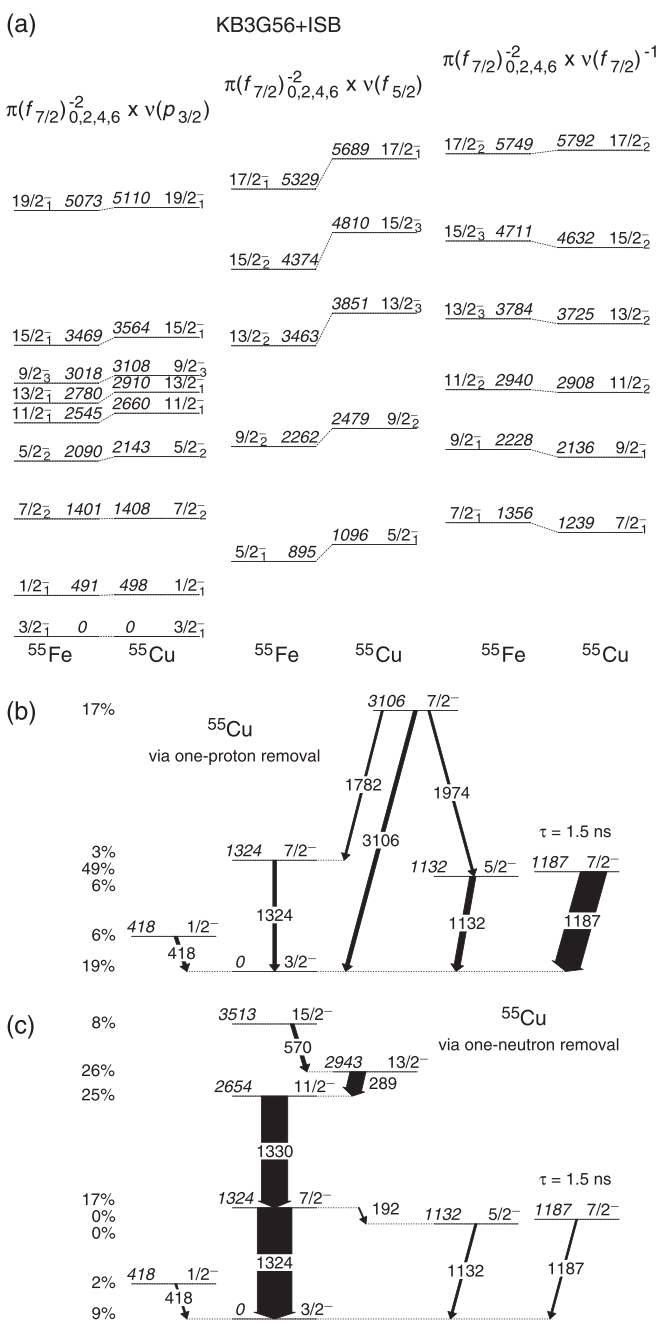

FIG. 7. Predictions for ^{55}Cu ($T_z = -3/2$) using the KB3G-based parametrization KB3G56-ISB as outlined in the text. Panel (a) provides a mirror energy comparison with calculated states in ^{55}Fe ($T_z = +3/2$). For the three subsets, the odd particle is in either the $p_{3/2}$, $f_{5/2}$, or $f_{7/2}$ orbital. Labels on top show the leading configurations for ^{55}Fe (see Fig. 6). Panel (b) provides a calculated decay scheme of ^{55}Cu following the population via one-proton removal from a radioactive ^{56}Zn beam. Panel (c) provides a calculated decay scheme of ^{55}Cu following the population via one-neutron removal from a radioactive ^{56}Cu beam. See text for details. Energy labels are in keV. In panels (b) and (c), percentages on the left-hand side indicate direct feeding from the respective reaction. The widths of the arrows correspond to the accumulated yield of the γ-ray transitions.

One-nucleon removal reactions of fast, secondary radioactive beams of either ^{56}Zn or ^{56}Cu should qualitatively lead to level schemes presented in Figs. 7(b) and 7(c), respectively. Direct and indirect feeding of states is accounted for, where only γ-ray transitions with a relative intensity exceeding 3% are shown.

Proton removal from ^{56}Zn probes primarily single-particle or single-hole character of low-spin states in ^{55}Cu, with a maximum of $I = 7/2$, by removing one $f_{7/2}$ proton from the 0^+ ground state of even-even ^{56}Zn. The corresponding $t = 6$ shell-model predictions are shown in Fig. 7(b), and corroborate this simple picture: The first three excited $7/2^-$ states are directly fed with relative yields of 49, 3, and 17%, respectively. The large number for the $7/2^-_1$ state at 1187-keV excitation energy simply reflects its $\pi(f_{7/2})^{-1}$ single-hole character. Similarly, the $5/2^-_1$, $1/2^-_1$, and $3/2^-_1$ states are populated by the proton-removal reaction with 6, 6, and 19%, respectively. This pattern is clearly consistent with their structural classification discussed earlier. It also follows by and large the ^{56}Zn ground-state occupation numbers. According to the predicted decay pattern, a ^{55}Cu γ-ray spectrum should thus be governed by a line with approximately 1.2 MeV, i.e., the $7/2^-_1 \rightarrow 3/2^-_1$ transition. With sufficient statistics and appropriate γ-ray energy resolution, basic mirror energy difference information for all states with $E_x < 1.5$ MeV could be probed; the other γ-ray transitions are expected to be about five to ten times weaker than the 1187-keV transition. A note of caution concerns the predicted ns isomerism of the $7/2^-_1$ level. Furthermore, in principle, single-particle removal reaction cross sections should be accounted for in the derivation of relative γ-ray yields as well, but this is unlikely to significantly change the observational *pattern* discussed above and shown in Fig. 7(b).

With ≈50%, the main partition of the predicted wave function of the 4^+ ground state of ^{56}Cu is $\pi(p_{3/2}) \times \nu(f_{7/2})^{-1}$. Consequently, producing ^{55}Cu via one-neutron removal will primarily populate states composed of sizable partitions of the $\pi(p_{3/2}) \times \nu(f_{7/2})^{-2}_{0,2,4,6}$ multiplet, i.e., states with spins up to $I = 15/2$. In fact, this pattern is recognized in the predicted level scheme shown in Fig. 7(c). About 85% of direct feeding enters the yrast cascade at spin $I = 15/2$, 13/2, 11/2, 7/2, and the $3/2^-$ ground state. The remaining 15% enter various yrare states, the decay of which cascades down in many branches, possibly leading to the observation of additional weak 418-, 1132-, and 1187-keV ground-state transitions. Here, a ^{55}Cu γ-ray spectrum should be governed by two intense peaks between 1.30 and 1.35 MeV, accompanied by an intense line at low energy, i.e., of 0.25–0.30 MeV, as well as a weaker line of 0.55–0.60 MeV, which corresponds to the $15/2^-_1 \rightarrow 13/2^-_1$ transition. In this case, once again with sufficient statistics and γ-ray energy resolution, the evolution of MED along the $\pi(p_{3/2}) \times \nu(f_{7/2})^{-2}_{0,2,4,6}$ structure could be tested, complementing the information expected from one-proton removal from ^{56}Zn.

A final note concerns discrete-energy proton emission from excited states of ^{55}Cu into states of ^{54}Ni. This decay

mode may compete with the electromagnetic decays described above. In fact, proton radioactivity was discovered in the $N = 26$ isotone ^{53}Co [58], and discrete-energy proton emission was observed in the isotope ^{58}Cu [59]. According to the most recent atomic mass evaluation, ^{55}Cu is proton unbound by 0.35(16) MeV [52], i.e., all states in ^{55}Cu can in principle decay by proton emission into the ground state of ^{54}Ni. Proton-emission decay widths are commonly factorized into a barrier penetration part of the emitted proton, $\Gamma_{\rm sp}$, and wave-function overlap by means of spectroscopic factors, C^2S. The latter follow from shell-model calculations; the former can be taken from semiclassical WKB estimates or proton scattering from, for instance, a Woods-Saxon potential [60]. The $3/2^-$ ground state of ^{55}Cu is known to β^+ decay with a half-life $T_{1/2} = 57(3)$ ms [61]. This implies that corresponding $Q_p \approx 0.3$ MeV, $\ell = 1$, $1p_{3/2}$ proton emission from the $7/2^-_2$ or $11/2^-_1$ states, which also belong to the $\pi(p_{3/2}) \times \nu(f_{7/2})^{-2}$ subset, into the 2^+_1 (1392 keV) or 4^+_1 (2620 keV) states in ^{54}Ni cannot compete with internal γ-ray decay, despite large spectroscopic factors. However, $Q_p \approx 1.6$ MeV, $\ell = 3$, $0f_{7/2}$ proton emission from the same states in ^{55}Cu, now into the 0^+_1 or the 2^+_1 states in ^{54}Ni, might be competitive, despite much reduced spectroscopic factors. At variance, direct $Q_p \approx 3.0$ MeV, $\ell = 5$, $0h_{11/2}$ proton emission from the $11/2^-_1$ state into the ground state of ^{54}Ni fails to compete with internal γ-ray decay because of the tiny spectroscopic factors associated with the $\mathcal{N} = 5$ orbital, which were recently assessed in case of ^{54}Ni proton radioactivity [62].

VII. SUMMARY AND CONCLUSIONS

The level scheme of ^{55}Fe has been significantly extended compared to previous studies and a few known inconsistencies have been resolved. Increased statistics and improved spectroscopic quality of data sets taken with Gammasphere coupled to detector systems for evaporated charged particles and neutrons were used. The observed low- to medium-spin states were grouped into three subsets, based on two-proton hole configurations combined with an unpaired neutron in either the $p_{3/2}$, $f_{5/2}$, or $f_{7/2}$ orbitals. A candidate for a noncollective $9/2^+$ intruder state was identified. A more satisfactory explanation for the highly excited side structures reported, as well as a more comprehensive study of the yrast line well above 10-MeV excitation energy, remain future tasks.

Comprehensive shell-model calculations were conducted for ^{55}Fe and excellent agreement was found for level energies and electromagnetic decay properties up to the third and eventually fourth state of a given spin. Accounting for isospin-breaking terms improves the theoretical description, taking advantage of the well-established KB3G interaction. Furthermore, an *ad hoc* adjustment of the gap size at particle number $N = Z = 28$ brought the $\nu(f_{7/2})^{-1}$ subset of states (and some yrast high-spin states) into the proper range of observed excitation energies. This calculation also improved the description of the electromagnetic decay properties further. Clearly, a more sustainable and profound, i.e., theoretical, adjustment of the gap size at ^{56}Ni of KB3G is due. This may be possible in a similar fashion as KB3G was made to evolve from KB3 [11], not the least to acknowledge the underlying realistic scope of the KB3 effective interaction. More recent spectroscopic data in the upper fp shell are available, including a number of states in $N \leqslant Z$ nuclei, which might aid such an update.

Based on the success of the adjusted KB3G56-ISB parametrization in describing the ^{55}Fe level scheme, a case study of its $T_z = -3/2$ mirror nucleus ^{55}Cu was conducted, including mirror energy differences and population and decay pattern for the possible production of ^{55}Cu via one-proton and one-neutron removal reactions. These predictions await spectroscopic data, which due to the complexity of the level scheme may be subject to future in-beam experiments at radioactive ion beam facilities exploiting the next generation of γ-ray tracking arrays GRETA [63] or AGATA [64] in conjunction with devices which are sensitive to prompt or delayed proton radioactivity.

ACKNOWLEDGMENTS

We would like to thank the accelerator crews and the Gammasphere support staff at ANL and LBNL, for their supreme efforts. This research used resources of ANL's ATLAS facility, which is a U.S. Department of Energy Office of Science User Facility. This work is supported in part by the Swedish Research Council (Vetenskapsrådet Grant No. VR 2016-3969) and the U.S. Department of Energy under Grants No. DE-AC02-05CH11231 (LBNL) and No. DE-AC02-06CH11357 (ANL).

[1] H. Grawe and M. Lewitowicz, Nucl. Phys. A **693**, 116 (2001).
[2] F. Nowacki, Nucl. Phys. A **704**, 223 (2002).
[3] T. Otsuka, M. Honma, and T. Mizusaki, Phys. Rev. Lett. **81**, 1588 (1998).
[4] D. Rudolph, C. Baktash, M. J. Brinkman, E. Caurier, D. J. Dean, M. Devlin, J. Dobaczewski, P.-H. Heenen, H.-Q. Jin, D. R. LaFosse, W. Nazarewicz, F. Nowacki, A. Poves, L. L. Riedinger, D. G. Sarantites, W. Satula, and C. H. Yu, Phys. Rev. Lett. **82**, 3763 (1999).
[5] E. K. Johansson, D. Rudolph, J. Ekman, C. Fahlander, C. Andreoiu, M. A. Bentley, M. P. Carpenter, R. J. Charity, R. M. Clark, P. Fallon, R. V. F. Janssens, F. G. Kondev, T. L. Khoo, T. Lauritsen, A. O. M. W. Reviol, D. G. Sarantites, D. Seweryniak, C. E. Svensson, and S. J. Williams, Eur. Phys. J. A **27**, 157 (2006).
[6] E. K. Johansson, D. Rudolph, L.-L. Andersson, D. A. Torres, I. Ragnarsson, C. Andreoiu, C. Baktash, M. P. Carpenter, R. J. Charity, C. J. Chiara, J. Ekman, C. Fahlander, C. Hoel, O. L. Pechenaya, W. Reviol, R. du Rietz, D. G. Sarantites, D. Seweryniak, L. G. Sobotka, C. H. Yu, and S. Zhu, Phys. Rev. C **77**, 064316 (2008).
[7] T. Mizusaki, T. Otsuka, M. Honma, and B. A. Brown, Phys. Rev. C **63**, 044306 (2001).
[8] D. Rudolph, B. G. Carlsson, I. Ragnarsson, S. Åberg, C. Andreoiu, M. A. Bentley, M. P. Carpenter, R. J. Charity, R. M. Clark, M. Cromaz, J. Ekman, C. Fahlander, P. Fallon, E.

Ideguchi, A. O. Macchiavelli, M. N. Mineva, W. Reviol, D. G. Sarantites, D. Seweryniak, and S. J. Williams, Phys. Rev. Lett. **96**, 092501 (2006).
[9] E. K. Johansson, D. Rudolph, I. Ragnarsson, L.-L. Andersson, D. A. Torres, C. Andreoiu, C. Baktash, M. P. Carpenter, R. J. Charity, C. J. Chiara, J. Ekman, C. Fahlander, O. L. Pechenaya, W. Reviol, R. du Rietz, D. G. Sarantites, D. Seweryniak, L. G. Sobotka, C. H. Yu, and S. Zhu, Phys. Rev. C **80**, 014321 (2009).
[10] M. Horoi, B. A. Brown, T. Otsuka, M. Honma, and T. Mizusaki, Phys. Rev. C **73**, 061305(R) (2006).
[11] A. Poves, J. Sánchez-Solano, E. Caurier, and F. Nowacki, Nucl. Phys. A **694**, 157 (2001).
[12] E. Caurier, G. Martínez-Pinedo, F. Nowacki, A. Poves, and A. P. Zuker, Rev. Mod. Phys. **77**, 427 (2005).
[13] M. Honma, T. Otsuka, B. A. Brown, and T. Mizusaki, Phys. Rev. C **65**, 061301(R) (2002).
[14] J. Ekman, C. Fahlander, and D. Rudolph, Mod. Phys. Lett. A **20**, 2977 (2005).
[15] M. A. Bentley and S. M. Lenzi, Prog. Part. Nucl. Phys. **59**, 497 (2007).
[16] D. Rudolph, C. Baktash, M. J. Brinkman, M. Devlin, H.-Q. Jin, D. R. LaFosse, L. L. Riedinger, D. G. Sarantites, and C. H. Yu, Eur. Phys. J. A **4**, 115 (1999).
[17] D. Rudolph, D. Weisshaar, F. Cristancho, J. Eberth, C. Fahlander, O. Iordanov, S. Skoda, Ch. Teich, O. Thelen, and H. G. Thomas, Eur. Phys. J. A **6**, 377 (1999).
[18] D. Rudolph, I. Ragnarsson, W. Reviol, C. Andreoiu, M. A. Bentley, M. P. Carpenter, R. J. Charity, R. M. Clark, M. Cromaz, J. Ekman, C. Fahlander, P. Fallon, E. Ideguchi, A. O. Macchiavelli, M. N. Mineva, D. G. Sarantites, D. Seweryniak, and S. J. Williams, J. Phys. G **37**, 075105 (2010).
[19] W. Reviol, D. G. Sarantites, R. J. Charity, V. Tomov, J. Dobaczewski, D. Rudolph, R. M. Clark, M. Cromaz, P. Fallon, A. O. Macchiavelli, M. P. Carpenter, and D. Seweryniak, Phys. Rev. C **65**, 034309 (2002).
[20] O. L. Caballero, F. Cristancho, D. Rudolph, C. Baktash, M. Devlin, L. L. Riedinger, D. G. Sarantites, and C.-H. Yu, Phys. Rev. C **67**, 024305 (2003).
[21] D. Rudolph, I. Ragnarsson, C. Andreoiu, M. A. Bentley, M. P. Carpenter, R. J. Charity, R. M. Clark, J. Ekman, C. Fahlander, P. Fallon, W. Reviol, D. G. Sarantites, and D. Seweryniak, Phys. Rev. C **102**, 014316 (2020).
[22] C. Langer, F. Montes, A. Aprahamian, D. W. Bardayan, D. Bazin, B. A. Brown, J. Browne, H. Crawford, R. H. Cyburt, C. Domingo-Pardo, A. Gade, S. George, P. Hosmer, L. Keek, A. Kontos, I-Y. Lee, A. Lemasson, E. Lunderberg, Y. Maeda, M. Matos *et al.*, Phys. Rev. Lett. **113**, 032502 (2014).
[23] W.-J. Ong, C. Langer, F. Montes, A. Aprahamian, D. W. Bardayan, D. Bazin, B. A. Brown, J. Browne, H. Crawford, R. Cyburt, E. B. Deleeuw, C. Domingo-Pardo, A. Gade, S. George, P. Hosmer, L. Keek, A. Kontos, I.-Y. Lee, A. Lemasson, E. Lunderberg *et al.*, Phys. Rev. C **95**, 055806 (2017).
[24] A. Fernández, A. Jungclaus, P. Doornenbal, M. A. Bentley, S. M. Lenzi, D. Rudolph, F. Browne, T. Koiwai, V. Vaquero, K. Wimmer, T. Arici, M. L. Cortés, N. Imai, N. Kitamura, B. Longfellow, R. Lozeva, B. Mauss, D. R. Napoli, M. Niikura, S. Periera Lopez, A. Poves, F. Recchia, P. Ruotsalainen, H. Sakurai, R. Taniuchi, S. Uthayakumaar, R. Wadsworth, and R. Yajzey (unpublished).
[25] Z. P. Sawa, Phys. Scr. **6**, 11 (1972).
[26] A. R. Poletti, B. A. Brown, D. B. Fossan, and E. K. Warburton, Phys. Rev. C **10**, 2312 (1974).
[27] H. Fromm, H. V. Klapdor, and P. Herges, J. Phys. G **7**, L109 (1981).
[28] M. G. Saint-Laurent, Sl. Cavallaro, M. L. Sperduto, B. Delaunay, J. Delaunay, and H. Dumont, Z. Phys. A **334**, 365 (1989).
[29] C. Keveloh, K. P. Lieb, and H. P. Hellmeister, Phys. Rev. C **26**, 716 (1982).
[30] P. G. Kerr, A. W. Gibb, and J. A. Cameron, Can. J. Phys. **51**, 707 (1973).
[31] H. Junde, Nucl. Data Sheets **109**, 787 (2008).
[32] https://www.nndc.bnl.gov/ensdf/, accessed 1 July 2021 for 55Fe.
[33] I.-Y. Lee, Nucl. Phys. A **520**, 641c (1990).
[34] D. G. Sarantites, P.-F. Hua, M. Devlin, L. G. Sobotka, J. Elson, J. T. Hood, D. R. LaFosse, J. E. Sarantites, and M. R. Maier, Nucl. Instrum. Methods Phys. Res., Sect. A **381**, 418 (1996).
[35] D. G. Sarantites, W. Reviol, C. J. Chiara, R. J. Charity, L. G. Sobotka, M. Devlin, M. Furlotti, O. L. Pechenaya, J. Elson, P. Hausladen, S. F. D. Balamuth, and R. M. Clark, Nucl. Instrum. Methods Phys. Res., Sect. A **530**, 473 (2004).
[36] J. Ekman, D. Rudolph, C. Andreoiu, C. Fahlander, M. N. Mineva, M. A. Bentley, S. J. Williams, R. J. Charity, E. Ideguchi, W. Reviol, D. G. Sarantites, V. Tomov, R. M. Clark, M. Cromaz, P. Fallon, A. O. Macchiavelli, M. P. Carpenter, and D. Seweryniak, Phys. Rev. C **70**, 014306 (2004).
[37] J. Ekman, PhD. thesis, Lund University, 2004.
[38] R. du Rietz, S. J. Williams, D. Rudolph, J. Ekman, C. Fahlander, C. Andreoiu, M. Axiotis, M. A. Bentley, M. P. Carpenter, C. Chandler, R. J. Charity, R. M. Clark, M. Cromaz, A. Dewald, G. de Angelis, F. Della Vedova, P. Fallon, A. Gadea, G. Hammond, E. Ideguchi, S. M. Lenzi, A. O. Macchiavelli *et al.*, Phys. Rev. C **72**, 014307 (2005).
[39] D. C. Radford, Nucl. Instrum. Methods Phys. Res., Sect. A **386**, 297 (1995).
[40] J. Theuerkauf, S. Esser, S. Krink, M. Luig, N. Nicolay, O. Stuch, and H. Wolters, program TV, University of Cologne (unpublished).
[41] C. E. Svensson, J. A. Cameron, S. Flibotte, G. Gervais, D. S. Haslip, J. M. Nieminen, J. C. Waddington, J. N. Wilson, G. C. Ball, A. Galindo-Uribarri, V. P. Janzen, D. C. Radford, D. Ward, M. Cromaz, and T. E. Drake, Nucl. Instrum. Methods Phys. Res., Sect. A **396**, 228 (1997).
[42] M. Devlin, L. G. Sobotka, D. G. Sarantites, and D. R. LaFosse, Nucl. Instrum. Methods Phys. Res., Sect. A **383**, 506 (1996).
[43] E. Caurier, shell model code ANTOINE, IRES, Strasbourg 1989–2002.
[44] E. Caurier and F. Nowacki, Acta Phys. Pol. **30**, 705 (1999).
[45] D. Rudolph, L.-L. Andersson, R. Bengtsson, J. Ekman, O. Erten, C. Fahlander, E. K. Johansson, I. Ragnarsson, C. Andreoiu, M. A. Bentley, M. P. Carpenter, R. J. Charity, R. M. Clark, P. Fallon, A. O. Macchiavelli, W. Reviol, D. G. Sarantites, D. Seweryniak, C. E. Svensson, and S. J. Williams, Phys. Rev. C **82**, 054309 (2010).
[46] S. M. Lenzi, M. A. Bentley, R. Lau, and C. Aa. Diget, Phys. Rev. C **98**, 054322 (2018).
[47] R. du Rietz, J. Ekman, D. Rudolph, C. Fahlander, A. Dewald, O. Möller, B. Saha, M. Axiotis, M. A. Bentley, C. Chandler, G. de Angelis, F. Della Vedova, A. Gadea, G. Hammond, S. M.

Lenzi, N. Mărginean, D. R. Napoli, M. Nespolo, C. Rusu, and D. Tonev, Phys. Rev. Lett. **93**, 222501 (2004).
[48] D. Rudolph, K. P. Lieb, and H. Grawe, Nucl. Phys. A **597**, 298 (1996).
[49] E. Stiliaris, H. G. Bohlen, X. S. Chen, B. Gebauer, A. Miczaika, W. von Oertzen, W. Weller, and T. Wilpert, Z. Phys. A **326**, 139 (1987).
[50] C. Andreoiu, D. Rudolph, I. Ragnarsson, C. Fahlander, R. A. E. Austin, M. P. Carpenter, R. M. Clark, J. Ekman, R. V. F. Janssens, T. L. Khoo, F. G. Kondev, T. Lauritsen, T. Rodinger, D. G. Sarantites, D. Seweryniak, T. Steinhardt, C. E. Svensson, O. Thelen, and J. C. Waddington, Eur. Phys. J. A **14**, 317 (2002).
[51] H. Junde, Nucl. Data Sheets **110**, 2689 (2009).
[52] M. Wang, W. J. Huang, F. G. Kondev, G. Audi, and S. Naimi, Chin. Phys. C **45**, 030003 (2021).
[53] J. R. Brown, M. A. Bentley, P. Adrich, D. Bazin, J. M. Cook, C. Aa. Diget, A. Gade, T. Glasmacher, S. M. Lenzi, S. McDaniel, B. Pritychenko, A. Ratkiewicz, K. Siwek, M. J. Taylor, and D. Weisshaar, Phys. Rev. C **80**, 011306(R) (2009).
[54] P. J. Davies, M. A. Bentley, T. W. Henry, E. C. Simpson, A. Gade, S. M. Lenzi, T. Baugher, D. Bazin, J. S. Berryman, A. M. Bruce, C. Aa. Diget, H. Iwasaki, A. Lemasson, S. McDaniel, D. R. Napoli, A. Ratkiewicz, L. Scruton, A. Shore, R. Stroberg, J. A. Tostevin, D. Weisshaar *et al.*, Phys. Rev. Lett. **111**, 072501 (2013).
[55] S. A. Milne, M. A. Bentley, E. C. Simpson, T. Baugher, D. Bazin, J. S. Berryman, A. M. Bruce, P. J. Davies, C. Aa. Diget, A. Gade, T. W. Henry, H. Iwasaki, A. Lemasson, S. M. Lenzi, S. McDaniel, D. R. Napoli, A. J. Nichols, A. Ratkiewicz, L. Scruton, S. R. Stroberg, J. A. Tostevin *et al.*, Phys. Rev. Lett. **117**, 082502 (2016).
[56] S. A. Milne, M. A. Bentley, E. C. Simpson, P. Dodsworth, T. Baugher, D. Bazin, J. S. Berryman, A. M. Bruce, P. J. Davies, C. Aa. Diget, A. Gade, T. W. Henry, H. Iwasaki, A. Lemasson, S. M. Lenzi, S. McDaniel, D. R. Napoli, A. J. Nichols, A. Ratkiewicz, L. Scruton, S. R. Stroberg *et al.*, Phys. Rev. C **93**, 024318 (2016).
[57] M. Spieker, A. Gade, D. Weisshaar, B. A. Brown, J. A. Tostevin, B. Longfellow, P. Adrich, D. Bazin, M. A. Bentley, J. R. Brown, C. M. Campbell, C. Aa. Diget, B. Elman, T. Glasmacher, M. Hill, B. Pritychenko, A. Ratkiewicz, and D. Rhodes, Phys. Rev. C **99**, 051304(R) (2019).
[58] J. Cerny, J. E. Esterl, R. A. Gough, and R. G. Sextro, Phys. Lett. B **33**, 284 (1970).
[59] D. Rudolph, C. Baktash, J. Dobaczewski, W. Nazarewicz, W. Satula, M. J. Brinkman, M. Devlin, H.-Q. Jin, D. R. LaFosse, L. L. Riedinger, D. G. Sarantites, and C. H. Yu, Phys. Rev. Lett. **80**, 3018 (1998).
[60] B. A. Brown (private communication); B. A. Brown and G. F. Bertsch, https://people.nscl.msu.edu/∼brown/reaction-codes/.
[61] Vandana Tripathi, S. L. Tabor, A. Volya, S. N. Liddick, P. C. Bender, N. Larson, C. Prokop, S. Suchyta, P.-L. Tai, and J. M. VonMoss, Phys. Rev. Lett. **111**, 262501 (2013).
[62] J. Giovinazzo, T. Roger, B. Blank, D. Rudolph, B. A. Brown, H. Alvarez-Pol, A. Arokia Raj, P. Ascher, M. Caamaño-Fresco, L. Caceres, D. M. Cox, B. Fernández-Domínguez, J. Lois-Fuentes, M. Gerbaux, S. Grévy, G. F. Grinyer, O. Kamalou, B. Mauss, A. Mentana, J. Pancin, J. Pibernat, J. Piot, O. Sorlin, C. Stodel, J.-C. Thomas, and M. Versteegen, Nat. Commun. **12**, 4805 (2021).
[63] GRETA (Gamma-Ray Energy Tracking Array) Conceptual Design Report, http://greta.lbl.gov/documents (2017).
[64] W. Korten, A. Atac, D. Beaumel, P. Bednarczyk, M. A. Bentley, G. B. A. Boston, A. Bracco, J. Cederkäll, B. Cederwall, M. Ciemala, E. Clément, F. C. L. Crespi, D. Curien, G. de Angelis, F. Didierjean, D. T. Doherty, Zs. Dombrádi, G. Duchêne, J. Dudek, B. Fernandez-Dominguez, B. Fornal *et al.* (AGATA Collaboration), Eur. Phys. J. A **56**, 137 (2020).